RESEARCH ARTICLE | DECEMBER 03 2025

Comparative analysis of the flow in a realistic human airway

Mario Rüttgers ; Julian Vorspohl ; Luca Mayolle ; Benedikt Johanning-Meiners ; Dominik Krug ; Michael Klaas ; Matthias Meinke ; Sangseung Lee ; Wolfgang Schröder ; Andreas Lintermann

Physics of Fluids 37, 121901 (2025)
https://doi.org/10.1063/5.0301891

Physics of Fluids ARTICLE pubs.aip.org/aip/pof

Comparative analysis of the flow in a realistic human airway

Cite as: Phys. Fluids **37**, 121901 (2025); doi: 10.1063/5.0301891
Submitted: 11 September 2025 · Accepted: 10 November 2025 ·
Published Online: 3 December 2025

Mario Rüttgers,[1,a] Julian Vorspohl,[2] Luca Mayolle,[2] Benedikt Johanning-Meiners,[2] Dominik Krug,[2] Michael Klaas,[2] Matthias Meinke,[2] Sangseung Lee,[1] Wolfgang Schröder,[2] and Andreas Lintermann[3,b]

AFFILIATIONS

[1]Data-Driven Fluid Engineering (DDFE) Laboratory, Inha University, Incheon 22212, Republic of Korea
[2]Institute of Aerodynamics and Chair of Fluid Mechanics (AIA), RWTH Aachen University, Aachen 52062, Germany
[3]Jülich Supercomputing Centre (JSC), Forschungszentrum Jülich GmbH, Jülich 52428, Germany

[a)]Electronic mail: m.ruettgers@inha.ac.kr
[b)]Author to whom correspondence should be addressed: a.lintermann@fz-juelich.de

ABSTRACT

Accurate simulations of the flow in the human airway are essential for advancing diagnostic methods. Many existing computational studies rely on simplified geometries or turbulence models, limiting their simulation's ability to resolve flow features such as shear-layer instabilities or secondary vortices. In this study, direct numerical simulations were performed for inspiratory flow through a detailed airway model that covers the nasal mask region to the sixth bronchial bifurcation. Simulations were conducted at two physiologically relevant Reynolds numbers with respect to the pharyngeal diameter, i.e., at $Re_p = 400$ (resting) and $Re_p = 1200$ (elevated breathing). A lattice-Boltzmann method was employed to directly simulate the flow, i.e., no turbulence model was used. The flow field was examined across four anatomical regions: (1) the nasal cavity, (2) the naso- and oropharynx, (3) the laryngopharynx and larynx, and (4) the trachea and carinal bifurcation. The total pressure loss increased from 9.76 Pa at $Re_p = 400$ to 41.93 Pa at $Re_p = 1200$. The nasal cavity accounted for the majority of this loss for both Reynolds numbers, though its relative contribution decreased from 81.3% at $Re_p = 400$ to 73.4% at $Re_p = 1200$. At $Re_p = 1200$, secondary vortices in the nasopharyngeal bend and turbulent shear layers in the glottis jet enhanced the local pressure losses. In contrast, the carinal bifurcation mitigated upstream unsteadiness and stabilized the flow. A key outcome is the spatial correlation between the pressure loss and the onset of flow instabilities across the four regions. This yields a novel perspective on how the flow resistance and vortex dynamics vary with geometric changes and flow rate.

I. INTRODUCTION

Understanding the flow physics of the airflow in the human airway is essential for applications ranging from inhalation therapy[9,14] and surgical planning[54,74] to modeling mechanical ventilators.[7] The complexity of the airway, which is characterized by intricate geometries with sharp bends and rapidly varying cross sections, gives rise to various flow phenomena, including laminar-to-turbulent transition, vortex formation, jet-like flow structures, recirculation zones, etc. Accurately resolving such features is critical for the analysis of, e.g., transport and deposition of aerosols,[35] predicting airway resistance to quantify respiration inhibition, or ultimately, for physics-based surgery decision making.[50,52]

The formation of flow structures is determined by the geometry and flow parameters. Despite the importance of the geometry, most studies focus on only a fraction of the airway, such as the nasal cavity,[33,46] glottis,[15,77] or trachea.[44,76] Furthermore, in many studies, simplified airway geometries such as straight-walled sections, idealized computer-aided design (CAD) segments, or even two-dimensional approximations are considered to facilitate meshing and reduce computational cost.[51,67] Comparative analyses reveal that these models often fail to capture essential flow features, including jets, recirculation zones, and regional deposition patterns.[2,10,26]

Numerical investigations frequently rely on solving the Reynolds-averaged Navier–Stokes (RANS) equations, including turbulence models, which are developed for different flow categories. Such computations are efficient;[57,66] however, they provide only low-resolution solutions of a temporally averaged flow field. In respiratory flow simulations, RANS simulations underperform in computing pressure drop[60]

and in representing turbulent fluctuations and oscillatory wall-shear stress (WSS), which are important to accurately predict aerosol transport and pathology-related flows.[8] Even though some scale-resolving, unsteady RANS simulations are able to reproduce the pressure drop in airways, they show weaknesses in capturing WSS fluctuations.[63] Thus, despite their efficiency, RANS methods contain modeling errors that are critical to study patient-specific airway dynamics and aerosol behavior.

Alternatively, large-eddy simulation (LES) and direct numerical simulation (DNS) offer a more detailed analysis of the underlying flow physics. LES resolves the large-scale turbulent eddies directly, and the small subgrid-scale motions are modeled. Hence, unsteady flow structures and spatial heterogeneities can be more accurately captured; however, at significantly higher computational cost compared to RANS simulations. In respiratory flows, LES has been used to understand complex flow features such as recirculation zones, shear-layer instabilities, and secondary vortices that are typically insufficiently resolved or misrepresented in RANS simulations.[6,30,80] Unlike LES methods, DNS resolves the entire spectrum of spatial and temporal flow scales without any modeling such that the "purest" flow field at an even higher computational cost will be determined.

Comparing numerical simulations of respiratory flows with experimental approaches such as particle image velocimetry (PIV) is crucial to validate numerical predictions.[76] For example, carefully checked numerical simulation software can be a powerful tool to characterize the deposition of inhaled particles in realistic geometries of the airway.[16,39,55] In other words, validation even for LES and DNS is necessary to ensure physical accuracy in patient-specific geometries. Thus, extensive high-fidelity simulations must be validated against *in vitro* or *in vivo* measurement data to confirm that complex flow structures determined in intricate geometries agree with experimental findings.

Additionally, airflow is frequently studied at a single flow rate, neglecting the variation introduced by different breathing intensities or activity levels.[23,32] Inhalation during exercise produces qualitatively and quantitatively significantly different flow dynamics from breathing at rest. These differences can strongly influence aerosol transport, pressure distributions, and shear stress distributions. For example, the peak velocity, wall pressure, and WSS can be up to nine times higher when running instead of walking.[71] Similarly, variations in the inhalation duration and respiratory rate cause substantial differences in secondary and lateral flow patterns even when peak REYNOLDS numbers are held constant.[18] Note that the REYNOLDS number is defined by the mean velocity, a relevant length scale, and the kinematic viscosity of air, i.e., it is proportional to the mean flow rate. The findings indicate that simulations at a single flow condition may miss critical variations in flow structures occurring in real-world respiratory scenarios, such as asymmetries or transitional turbulence, that are important to accurately predict drug delivery, airway collapse risk, patient-specific treatment planning, etc. Therefore, a comprehensive analysis should include multiple breathing conditions, e.g., rest and exertion, to cover the functional range of the airway physiology and to validate computational fluid dynamics (CFD) simulations appropriately.

The current study addresses the previously mentioned limitations. DNS of steady flow at nasal inhalation for a realistic, adult human airway geometry from a mask covering the nostrils to the sixth bronchial bifurcation is performed. Simulations are conducted at the REYNOLDS numbers $Re = 400$ and $Re = 1200$ to capture the flow structures of peak inhalation conditions under resting and moderately increased breathing. The DNS is based on a high-fidelity lattice-Boltzmann (LB) method using 435×10^6 cells such that a fully resolved representation of the unsteady flow phenomena is achieved. The LB method is part of the open-source simulation framework multiphysics-Aerodynamisches Institut Aachen (m-AIA).[1] It has been used for numerous numerical investigations of nasal cavity flows, such as thermal analyses of patients' breathing capabilities,[33,36,73] machine learning-based automatization of pre-processing and executing CFD simulations,[37,53,72] and automated virtual surgery planning for treating respiratory diseases.[50,52,54]

The DNS results are validated against high-resolution experimental data measured in the same geometry under steady flow conditions. The experiments were performed using a surface-coated biological model and a colorimetric 3-(4,5dimethylthiazol-2-yl)-2,5-diphenyltetrazolium bromide (MTT) assay to determine the aerosol deposition in the airways. First, high-speed mono-PIV measurements were conducted to determine the relationship between the flow field and the aerosol deposition.[25] Second, to investigate the influence of oral and nasal inhalation on the lower airways at peak in- and exhalation, 3D particle-tracking velocimetry (3D-PTV) measurements using the shake-the-box (STB) algorithm were performed.[24]

While the experimental investigations are limited to accessible regions, DNS yields data for the entire domain, revealing flow features not observable in the experiments. To the best of the authors' knowledge, this is the first validated DNS study of the complex airflow in a realistic human airway model covering the full inhalation path down to the sixth bifurcation at two REYNOLDS numbers. The results highlight how vortical structures emerge, interact, and evolve across anatomical boundaries. Transition mechanisms and secondary flow features that are absent or not resolved in previous studies are discussed. A further novel aspect of this study is the systematic, region-by-region correlation analysis of the pressure loss, which is complemented by considering flow instabilities and transitional behavior. This comprehensive analysis offers a new perspective on how geometry and flow rate influence respiratory airflow and is a further step for improved physiological modeling and diagnostic approaches.

This manuscript is structured as follows. Section II presents the airway geometry, the experimental and numerical techniques, and a mesh refinement study. In Sec. III, the numerical results are compared to experimental data, and the flow field in the four key anatomical regions is analyzed. Then, the results are summarized, discussed, and an outlook is given in Sec. IV.

II. METHODS

The airway geometry (Sec. II A), experimental techniques (Sec. II B), and the numerical methods, including the boundary conditions and a mesh refinement study (Sec. II C) are presented.

A. Geometry

The analysis in this study focuses on the development and evolution of flow structures in the following four key anatomical regions, which are highlighted by different colors in Fig. 1:

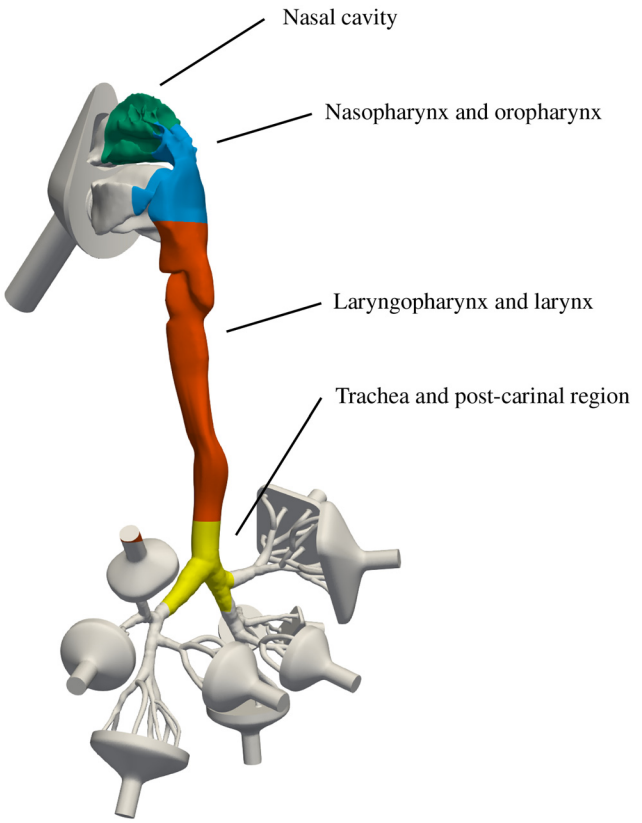

FIG. 1. Key anatomical regions investigated in this study.

- The nasal cavity (green), which is characterized by narrow valve regions and turbinate-induced flow acceleration with complex, multiscale recirculation.
- The naso- and oropharynx (blue), where curvature-induced vortex pairs develop due to the nasal–pharyngeal transition.
- The laryngopharynx and larynx (red), featuring shear-layer instabilities and jet-like behavior frequently referred to as "glottis jet."
- The trachea and post-carinal regions (yellow), where downstream stabilization and interaction of secondary vortices occur.

The present airway geometry[16,39] originates from a lung model developed at the Brno University of Technology and is derived from a three-dimensional computed tomography (CT) scan of an adult Caucasian male.[38] It includes the oral cavity, larynx, and tracheobronchial tree down to the seventh generation. To enable the investigation of airflow and particle deposition during nasal, oral, and combined breathing, the model was extended by incorporating a nasal cavity obtained from the University of California, Davis.[58] The nasal geometry was derived from CT scans of a healthy 25-year-old male and post-processed using Rhinoceros 3D[42] and Star-CCM+[65] to remove unwanted paranasal sinuses and to smooth the surface. The nasal and oral cavities were subsequently connected according to anatomical references[47] to ensure realistic proportions, positioning, and morphology. Individual nasal inhalation was realized by sealing the oral cavity

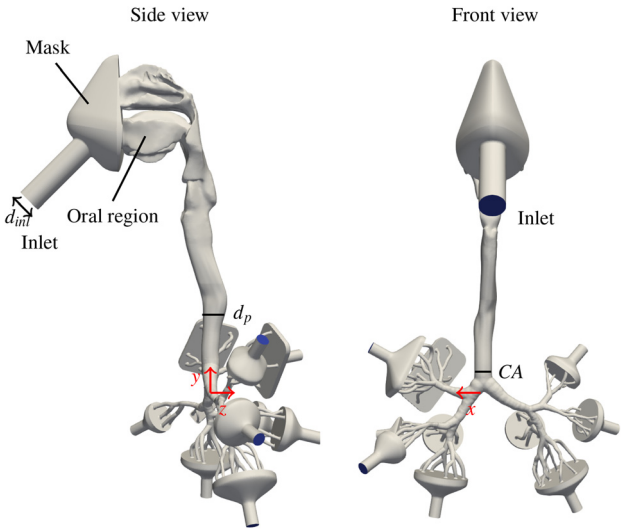

FIG. 2. The computational domain and its geometric details.

with an especially designed plug, manufactured using the lost-core technique and derived from the overall airway geometry. Finally, the 52 outlets of the sixth bifurcation generation were merged into ten funnels.

The computational domain and the coordinate system are illustrated in Fig. 2. The nostrils and mouth are covered by a mask that is extended by a pipe with an inlet diameter of $d_{inl} = 20$ mm. The connection between the mask and the oral region is closed, and only nasal breathing is considered. The pipe has an inclination angle of $\alpha = 45°$. The ten outlets have diameters of $d_{outl} = 8$ mm. The REYNOLDS number at the pharynx $Re_p = (U_p \cdot d_p)/\nu$ is based on the hydraulic diameter of the pharynx region $d_p = 16.3$ mm at $y = 2.92 \cdot d_p$, the kinematic viscosity ν, and the spatially averaged velocity at the pharynx U_p. The hydraulic diameter at the pharynx is computed by $d_p = 4A_p/C_p$, where A_p and C_p are the cross-sectional area and circumference at the pharynx. The REYNOLDS number at the inlet is defined as $Re_{inl} = (U_{inl} \cdot d_{inl})/\nu$. The spatially averaged inflow velocity U_{inl} is determined by the mass conservation equation $U_{inl} \cdot A_{inl} = U_p \cdot A_p$, where A_{inl} is the cross-sectional area at the inlet.

To match the measurements of Johanning-Meiners *et al.*,[24,25] results for $Re_p = 400$ and $Re_p = 1200$ are investigated. Under resting physiological conditions, the tidal volume per breathing cycle is approximately 500 ml. The corresponding, i.e., calm breathing frequency in ambient air is typically around 0.1 Hz, yielding an average volume flux on the order of 300 l h^{-1}. This translates to a characteristic REYNOLDS number in the trachea of approximately $Re_p = 400$ under resting conditions. When transitioning to moderate breathing, the increased tidal volume and breathing rate raise the flow velocity, leading to a higher REYNOLDS number of about $Re_p = 1200$. At both flow rates, unsteady (pulsatile) effects can be considered negligible. Studies have shown that, during calm breathing, i.e., WOMERSLEY numbers up to one, oscillatory flow fields do not differ significantly from the corresponding steady flow fields, and no shear-related temporal phenomena occur during flow reversal.[17]

TABLE I. Quantities ρ, ν, U_p, and U_{inl} for different fluids and REYNOLDS numbers.

			$Re_p = 400\ (I)$		$Re_p = 1200\ (II)$	
Fluid	ρ (kg m^{-3})	ν (m^2 s^{-1})	U_p^I (m s^{-1})	U_{inl}^I (m s^{-1})	U_p^{II} (m s^{-1})	U_{inl}^{II} (m s^{-1})
Air	1.17	1.63×10^{-5}	0.40	0.27	1.20	0.81
Water + glycerin	1139	5.44×10^{-6}	0.13	0.09	0.39	0.27

B. Experimental methods

The experiments were carried out using a silicone model of the human respiratory tract integrated into a closed-circuit system simulating steady inhalation. The model was cast from RTV-615 silicone with a Shore A hardness of approximately 44. The quantities ρ, ν, U_p, and U_{inl} for the water and glycerin fluid are summarized in Table I. The experimental setup is sketched in Fig. 3. The silicone's model refractive index $n = 1.406$ was matched by a mixture of water (56.75 wt. %) and glycerin (43.25 wt. %), which was held constant during all the experiments at a temperature of 30 °C using heating plates that were actively controlled by a proportional integral derivative (PID) controller. The mixture yields a density of $\rho_{WG} = 1139$ kgm^{-3} and a dynamic viscosity of $\eta_{WG} = 0.006$ Pas. The wall thicknesses of the upper airways, trachea, and bronchial tree were in the range of $8\,\text{mm} < \delta < 100\,\text{mm}$, resulting in a quasi-rigid, non-compliant airway replica.

A fully developed inlet velocity profile was generated using an inlet pipe with the length $L_{inl} = 82 \cdot d_{inl}$ including a flow straightener downstream of the pump. The minimum pipe length required to achieve a fully developed laminar flow was estimated for $Re_p = 1200$, corresponding to an inlet REYNOLDS number of $Re_{inl} = 993$. Since laminar conditions are maintained for $Re_{inl} < 2000$,[49] the flow remained in the laminar regime for the present configuration. Following the empirical correlation $L_e = 0.06 \cdot Re_{inl} \cdot d_{inl}$,[61] the minimum entrance length was estimated as $L_e = 59 \cdot d_{inl}$. Accordingly, a total pipe length of $82 \cdot d_{inl}$ ensured that the flow was fully developed at the inlet.

Two independent PIV systems were used in the experiments. For the first system, the velocity profile upstream of the mask and thus the REYNOLDS number in the trachea was measured using a Continuum Minilite low-speed laser combined with a pco.edge sCMOS camera. Two-dimensional velocity fields were captured using a Darwin-Duo 40 mJ laser and a Photron FASTCAM NOVA S12, achieving a spatial resolution of 17 px mm^{-1}. The raw images were processed using an in-house cross correlation algorithm and the method is further referred to as PIV. For the STB measurements, the FASTCAM NOVA S12 and two additional Photron FASTCAM Mini WX100 cameras were equipped with a 100 mm Zeiss lens and positioned at an angle of 0° and 25°, respectively, each at a distance of approximately 800 mm from the measurement volume.

To further minimize the distortion of the cameras, the measurement tank was built such that the walls were perpendicular to each camera, and the FASTCAM Mini WX100 cameras were Scheimpflug corrected, resulting in a final spatial resolution of 19.5 px mm^{-1}. An Nd:YLF Darwin-Duo laser (100 mJ) with a wavelength of $\lambda = 527$ nJ was equipped with volumetric light-sheet optics (LaVision) to illuminate the measurement volume within the trachea. The resulting illuminated region measured approximately $25 \times 25 \times 50$ mm^3. For the two REYNOLDS numbers, a single exposure frequency of 619 and 1806 Hz was used. The water/glycerin mixture was seeded with Orgasol particles, often used in STB applications[62] with a mean diameter of 47.7 μm, resulting in a maximum STOKES number of $Sto_{max} = 5 \times 10^{-4}$. Due to the three-camera setup used in the measurements, a lower seeding density of approximately 0.03 ppp was used for all experiments. The images obtained from the three cameras were processed in DaVis 10 by LaVision using the STB algorithm.[59]

A 3D calibration target, namely, LaVision Type 11 was used to map the camera pixels to the real-world coordinates. Hence, the target was placed inside the measurement tank filled with the water/glycerin mixture without the model at three equidistant axial positions with a spacing of 10 mm and the mapping was performed via refractive index matching. Each camera was first focused on the calibration target positioned at $z = 0$ using a low depth of field (small f-number). Then, the target was removed and the airway model was positioned inside the tank. Subsequently, the depth of field was increased to fully capture the entire measurement volume during the experiments. Next, the calibration target was reinserted under these same optical settings to perform the calibration procedure.

The mapping was obtained using a third-order polynomial fit, followed by a volume self-calibration routine. The volume self-calibration was conducted with the same particle density (approximately 0.03 ppp), frame rate, and exposure as in the experiments. The self-calibration was performed iteratively until the maximum disparity error was reduced below 0.1 *vx*, ensuring subpixel accuracy. To maintain reproducibility during calibration and measurements, the airway model was held in the same position by brackets. The same routine was applied for the calibration target such that the $z_{calib} = 0$ reference plane was located in the center of the tracheal lumen. The volume self-calibration resulted in a final maximum calibration fit error of 0.0099 *px* for the cameras. To enhance the quality of the raw images, a pre-processing routine was applied by subtracting a robust moving average from each image and applying a geometric mask. For the processing of the STB measurements, a triangulation error of 1.5 *vx*, a

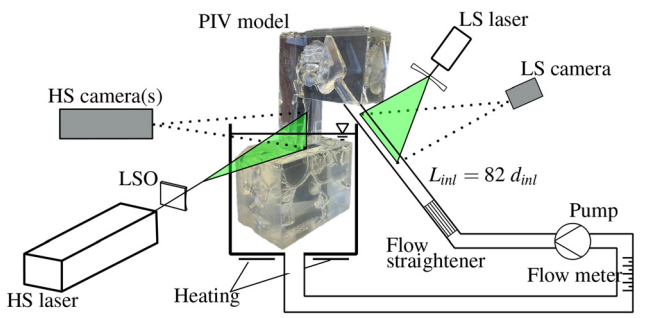

FIG. 3. Sketch of the experimental setup for PIV and 3D-PTV measurements.

shake width of 0.11 *vx*, a particle intensity threshold of $0.1I_{avg}$, where I_{avg} denotes the average image intensity per camera, and a minimum track length of six steps were employed to reduce ghost particles. Finally, a spatial median $3 \times 3 \times 3$ filter was applied to further reduce false particle tracks. Since no ensemble averaging approach was utilized, preliminary testing showed that a seeding density of approximately 0.03 *ppp* yielded the best results.

Due to the nature of the experimental setup, i.e., the model was submerged in a tank filled with the water/glycerin mixture, a laser was used instead of a light-emitting diode (LED) system to more precisely guide the light beam onto the measuring section. An additional cross validation of the STB measurements with the PIV results can be found in Ref. 24.

C. Numerical methods

The numerical simulations were conducted on the central processing unit (CPU) partition on the JURECA-DC supercomputer[69] of the Jülich Supercomputing Centre (JSC), Forschungszentrum Jülich, Germany. Each node contains two AMD EPYC 7742 processors with 64 cores each, clocked at 2.25 GHz, and 512 GB DDR4 memory.

The LB method implemented within the m-AIA framework was employed. The LB approach is particularly advantageous for handling highly complex and detailed geometries.[19] The LB module solves the discretized form of the Boltzmann equation with the Bhatnagar–Gross–Krook (BGK) approximation of the right-hand side collision process.[22] That is

$$f_i(\boldsymbol{x} + \boldsymbol{\xi_i}\delta t, t + \delta t) - f_i(\boldsymbol{x}, t) = -\omega(f_i(\boldsymbol{x}, t) - f_i^{eq}(\boldsymbol{x}, t)), \quad (1)$$

is solved for the particle probability distribution functions f_i at neighboring fluid cells at locations $\boldsymbol{x} + \boldsymbol{\xi_i}\delta t$. The PPDFs are functions of the location vector $\boldsymbol{x} = (x, y, z)^T$, the discrete molecular velocity vector $\boldsymbol{\xi}_i = (\xi_1, \xi_2, \xi_3)^T$, and the time t and the time increment δt. The collision frequency is expressed by ω. The discretization is based on the D3Q27 model,[48] with $i \in \{1, \ldots, Q = 27\}$ directions in 3D. The discrete Boltzmann–Maxwell distribution function reads

$$f_i^{eq} = w c_i \rho \left(1 + \frac{\boldsymbol{\xi_i} \cdot \boldsymbol{u}}{c_s^2} + \frac{1}{2}\left(\frac{\boldsymbol{\xi_i} \cdot \boldsymbol{u}}{c_s^2}\right)^2 - \frac{\boldsymbol{u} \cdot \boldsymbol{u}}{2c_s^2}\right), \quad (2)$$

with the isothermal speed of sound $c_s = 1/\sqrt{3}$, fluid density ρ, fluid velocity vector $\boldsymbol{u} = (u, v, w)^T$ with the velocity components u, v, and w in the x-, y-, and z-directions, and weight coefficients wc_i.[48]

The macroscopic variables ρ and $\boldsymbol{u}$ can be computed by

$$\rho = \sum_{i=1}^{Q} f_i, \quad (3)$$

$$\rho \boldsymbol{u} = \sum_{i=1}^{Q} \boldsymbol{\xi}_i \cdot f_i. \quad (4)$$

Following the isothermal equation of state, the relation between static pressure and density fluctuations can be expressed as $p'_{stat} = c_s^2 \rho'$. The static pressure is then obtained by $p_{stat} = p_0 + p'_{stat} = p_0 + c_s^2(\rho - \rho_0)$, where p_0 and ρ_0 are the reference pressure and density. Since the LB method is mimicking the incompressible Navier–Stokes equations, the actual pressure level is chosen during post-processing. The total pressure reads $p_{tot} = p_{stat} + p_{dyn}$, with the dynamic pressure $p_{dyn} = \rho u_{mag}^2/2$ and the velocity magnitude $u_{mag} = \sqrt{u^2 + v^2 + w^2}$.

At the inlet, the parabolic velocity profile of a fully developed laminar pipe flow is prescribed, and the density of the fluid is linearly extrapolated from the neighboring inner cells. At all outlets, the constant density $\rho_{outl} = \rho_0 = 1$ (in lattice units) is set, which corresponds to a constant pressure. Since a single pressure value is physically not meaningful, pressure differences are considered. The static pressure differences between two locations (1 and 2) in lattice units can be expressed as $p_{stat,2} - p_{stat,1} = c_s^2(\rho_2 - \rho_1)$, which becomes $(p_{stat,2} - p_{stat,1})_{phys.} = (\rho_{phys.} U_{inl}^2)/(\rho_0 Ma^2)(\rho_2 - \rho_1)$ in physical units. The total pressure difference in physical units analogously reads $(p_{tot,2} - p_{tot,1})_{phys.} = (\rho_{phys.} U_{inl}^2)/(\rho_0 Ma^2)(\rho_2 - \rho_1 + \rho_2 u_{2,mag}^2 - \rho_1 u_{1,mag}^2)$. The dimensional pressure differences are computed with the values of the quantities ρ and U_{inl} for air, which are given in Table I. To satisfy the no-slip condition on the walls, an interpolated bounce-back scheme is used.[5]

Unstructured, hierarchical Cartesian meshes with uniform refinement are generated using the massively parallel mesh generator integrated in the m-AIA framework.[34] The mesh has an octree data structure, which is created by recursively subdividing an initial bounding cube that encloses the region of interest (ROI),[21] i.e., the airway. On each refinement level parent cubes are divided into eight smaller sub-cubes, forming a hierarchical structure through well-defined parent–child relationships. Cells outside the ROI are discarded to reduce computational overhead and to optimize the mesh.

The mesh is refined up to a predefined level, which is used to perform domain decompositioning with a Hilbert space-filling curve.[56] Cells on lower refinement levels are ordered using a Z-curve (Morton order).[45] Concerning parallel processing, the Hilbert curve preserves spatial locality, ensuring that neighboring cells in the domain are typically assigned to the same or adjacent computational processes. This, together with the Z-curve on a sub-domain level, promotes efficient data locality both within and across compute nodes, minimizing communication overhead. Since the domain partitioning is balanced from the outset and remains static, load imbalance does not occur under uniform refinement. The final mesh is stored using the parallel Network Common Data Form (NetCDF) and written via concurrent I/O routines,[31] enabling scalable and efficient data handling for large simulations.

Simulations with a coarse (subscript *c*), medium (subscript *m*), and fine (subscript *f*) mesh at $\Delta x_c = d_{inl}/50$ with 7×10^6 cells, $\Delta x_m = d_{inl}/100$ with 55×10^6 cells, and $\Delta x_f = d_{inl}/200$ and 433×10^6 cells have been conducted, where Δx represents the cell size. Figure 4 provides cross-sectional views for the different mesh resolutions at the location indicated in the sketches. The nasal cavity was chosen for illustration because it represents the narrowest region with the most demanding mesh requirements. Uniformly refined Cartesian meshes were used such that the grid spacing is constant throughout the domain. Accordingly, additional mesh visualization locations do not provide further information.

Figure 5 shows the results of a mesh refinement study at $Re_p = 400$ and $Re_p = 1200$. The results are shown in the form of nine equidistant cross sections in the x–z plane ranging from $y/d_p = 4$ to $y/d_p = 6.4$. This region is highlighted by the black area in the 3D model shown on the left side. The cross sections are colored by the normalized absolute velocity u_{mag}/U_p. All cross sections show a

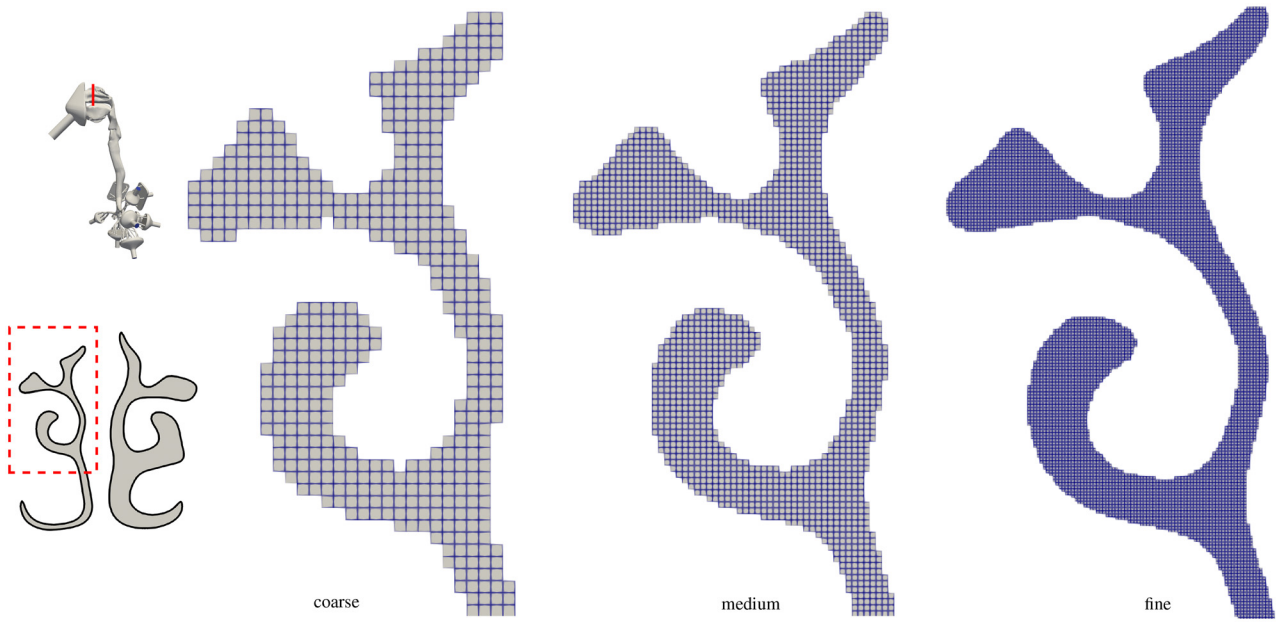

FIG. 4. Cross-sectional view at the location indicated in the sketches, illustrating the grid resolution of the coarse, medium, and fine meshes in the most constricted region of the geometry.

high-speed jet in the center. For $Re_p = 400$, the coarse simulation computes a lower velocity magnitude in the center of the jet compared to the medium and fine simulations. In the medium and fine simulations, the jet develops a dented shape from the center in the positive z-direction. In the coarse simulation, this dented shape of the jet is only indicated in the upper two cross sections. In the remaining cross sections, this structure is no longer observed. Furthermore, while the low-velocity part of the jet extends into the center of the cross sections in the medium and fine simulations, it is only present near the wall in the coarse simulation. In other words, the coarse resolution is not sufficient to capture even such large-scale flow features. However, the simulations based on the medium and fine meshes do resolve the dented shape and the low-velocity part, which extends into the center in all cross sections. Differences between the medium and fine simulations are hardly visible. This indicates a qualitative convergence of the flow features with increasing mesh resolution.

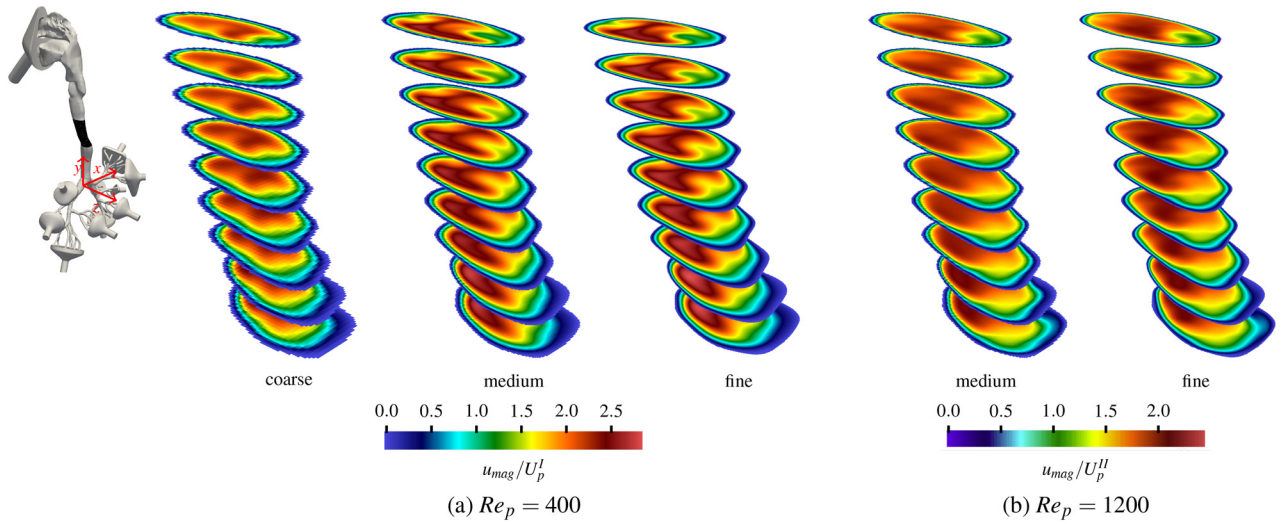

FIG. 5. Equidistant cross sections of the normalized velocity magnitude u_{mag}/U_p at two Reynolds numbers in the x–z plane ranging from $y/d_p = 4$ to $y/d_p = 6.4$, which is highlighted by the black area in the 3D model. Results for various mesh resolutions are juxtaposed.

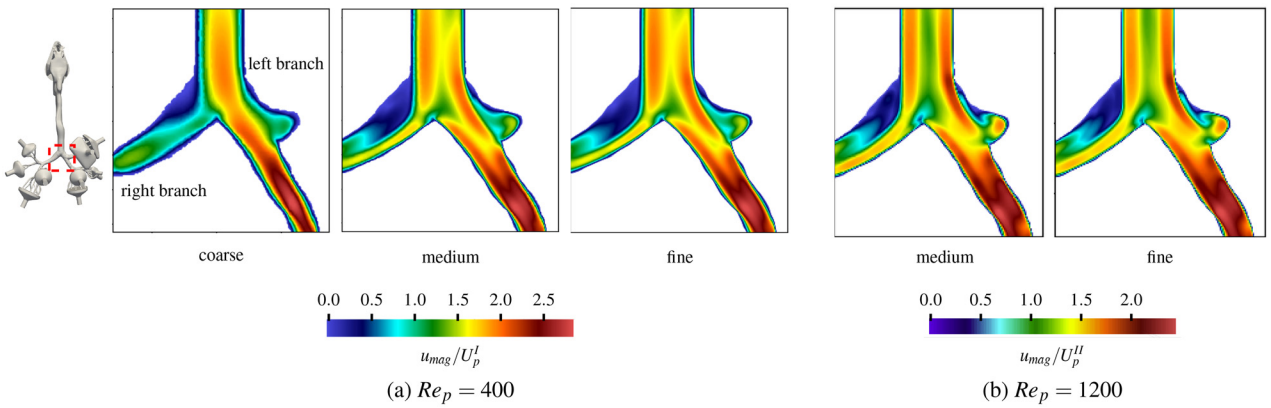

(a) $Re_p = 400$ (b) $Re_p = 1200$

FIG. 6. Contours of the normalized velocity magnitude u_{mag}/U_p in the bifurcation (dashed red square at $z = 0$ in the sketch). Results for various mesh resolutions are juxtaposed.

For $Re_p = 1200$, only the results for the medium and fine simulations are shown since the results for the coarse simulation were not reliable. Unlike the $Re_p = 400$ case, where the slowly flowing part extended into the center for all cross sections, for $Re_p = 1200$, this is only observed for the first three cross sections. It can be stated that only slight differences between the medium and fine simulations are observed. These small differences suggest that the results are qualitatively converged with respect to the mesh resolution.

Next, the flow field at the bifurcation in a cross section at $z = 0$ and for $x, y \in [-30\,\text{mm}, 30\,\text{mm}]$ is assessed. Figure 6 shows the comparison for $Re_p = 400$ again for the coarse, medium, and fine resolutions. Upstream of the bifurcation, the medium and fine simulations clearly show two maxima in the velocity profile. They are not visible in the coarse simulation since the numerical diffusion dampens the development of such a flow structure. In the right branch of the bifurcation, all simulations show a clear flow separation and a recirculation zone that is covered by a thin wall jet. However, the wall jet following the impingement is larger and the size of the recirculation zone smaller in the coarse simulation compared to the medium and fine ones. In the left branch, the coarse simulation predicts a centered jet, while the medium and fine simulations show two wall jets that merge into one jet downstream. The close agreement between the medium and fine simulations indicates again that the main flow structures are qualitatively converged.

For the $Re_p = 1200$ problem, again only the medium and fine grid results are shown. The overall flow structure is comparable to the case of $Re_p = 400$. For the right branch of the bifurcation, the wall jet is noticeably wider at $Re_p = 1200$, which is due to the somewhat smaller and thinner separation bubble. As for the lower REYNOLDS number case, the similarity between the medium and fine results demonstrates a qualitative convergence of the predicted flow field.

Figure 7 shows velocity profiles along the line "CA" (see Fig. 2), in the x-direction at $y/d_p = 0.85$ and $z/d_p = 0.0$ for different mesh resolutions. For $Re_p = 400$, all simulations exhibit two local maxima along the profile. In the coarse simulation, only the first peak agrees well with the medium and fine simulations, whereas the second peak is

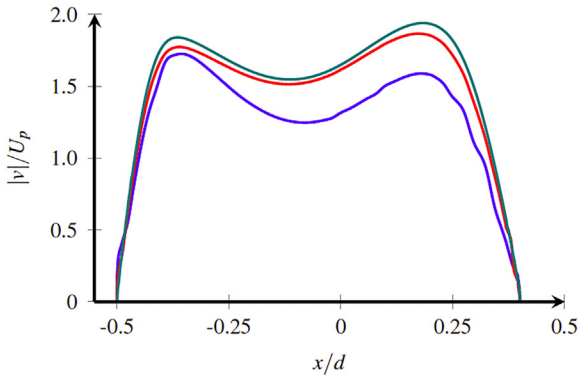

(a) $Re_p = 400$.

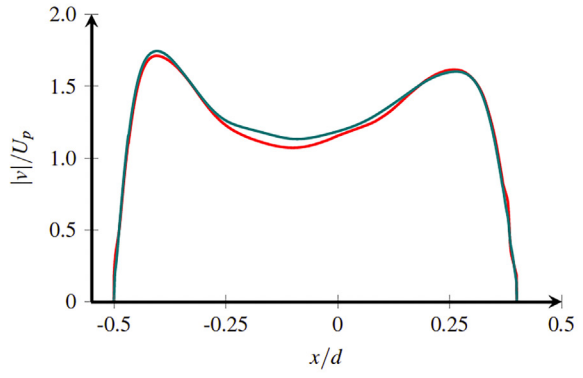

(b) $Re_p = 1200$.

FIG. 7. Profiles of $|v|/U_p$ along the line "CA" (see Fig. 2), in the x-direction at $y/d_p = 0.85$ and $z/d_p = 0.0$ forthe coarse (blue), medium (red), and fine (green) meshes.

significantly underpredicted. The velocity profiles of the medium and fine simulations, on the other hand, show good agreement across the entire line. The mean deviation between the coarse and medium profiles, normalized by the mean velocity along the profile of the medium case, is 13.7%, while the mean deviation between the medium and fine profiles, normalized by the mean velocity along the profile of the fine case, is 3.9%. These results demonstrate a quantitative convergence of the velocity field with increasing mesh resolution.

For $Re_p = 1200$, the comparison focuses on the medium and fine simulations. Similar to the lower REYNOLDS number case, two local maxima are observed along the velocity profile. The mean deviation between the medium and fine simulations is only 2.7%.

Based on the qualitative and quantitative assessments discussed above, the simulations conducted with the fine mesh can be considered sufficiently resolved to capture all relevant flow features. The differences between the medium and fine meshes are minor across all investigated flow quantities and locations, confirming mesh independence within the expected level of numerical accuracy. Therefore, the results obtained with the fine mesh are used for all subsequent analyses and discussions in this study.

In Sec. III, the Q-criterion is analyzed, which is given by

$$Q = \frac{1}{2}(\Omega_{jk}\Omega_{jk} - \Psi_{jk}\Psi_{jk}), \tag{5}$$

where Ψ_{jk} is the symmetric rate-of-strain tensor, Ω_{jk} is the anti-symmetric rate-of-rotation tensor, and $j, k \in \{1, 2, 3\}$ are spatial coordinate indices in the x-, y-, and z-directions.[13] To visualize vortical structures, iso-surfaces of the normalized Q-criterion in regions where

$$Q_{norm}^{min} < \frac{Q}{(U_{inl}/d_{inl})^2} < Q_{norm}^{max} \tag{6}$$

are displayed. The lower and upper limits $Q_{norm}^{min} = -3.5 \times 10^4$ and $Q_{norm}^{max} = 3.5 \times 10^4$ are based on physically meaningful flow scales to highlight dynamically significant vortices while suppressing background noise.

To analyze the dominant frequency content of the unsteady flow in Sec. III, the normalized spectral energy (E_{norm})

$$E_{norm} = \frac{(u'u' + v'v' + w'w')}{U_{inl}^2} \tag{7}$$

is evaluated as a function of the nondimensional STROUHAL number (St)

$$St = \frac{fr \cdot d_{inl}}{U_{inl}}, \tag{8}$$

where u', v', and w' denote the fluctuating velocity components, and fr is the temporal frequency obtained from the Fourier transform of velocity signals recorded at point probes within the flow field. The probe data are sampled at every time step, providing sufficiently high temporal resolution to resolve the relevant oscillation modes. This representation enables direct comparison of the energy distribution across frequencies and flow regimes.

The centerlines for analyzing the distribution of the total pressure in Sec. III are computed using the Vascular Modeling Toolkit (VMTK).[3] The normal vector of a cross section through a point s on the centerline is computed based on two consecutive locations along the centerline. The area of a cross section is determined by a region-growing algorithm whose seed point is located at s.

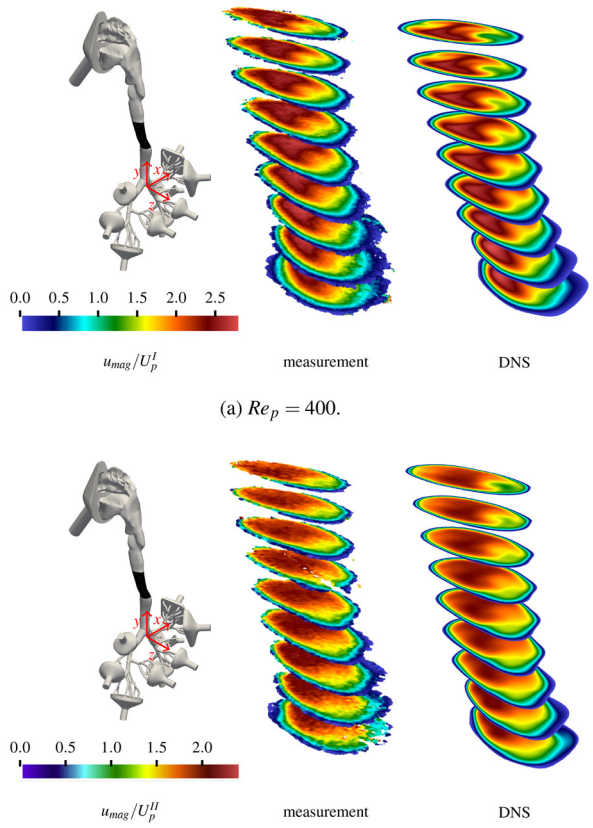

(a) $Re_p = 400$.

(b) $Re_p = 1200$.

FIG. 8. Equidistant cross sections of the normalized velocity magnitude u_{mag}/U_p at two REYNOLDS numbers in the x–z plane ranging from $y/d_p = 4$ to $y/d_p = 6.4$, which is highlighted by the black area in the 3D model on the left. Results of the DNS are compared to excerpts of the 3D-PTV measurement series described in Ref. 24.

III. RESULTS

In Sec. III A, a validation with the experimental measurements is presented. Section III B provides a detailed analysis of flow structures in the four key anatomical regions, see Fig. 1, including the effect of the different REYNOLDS numbers on the flow fields. In Sec. III C, the influence of the different flow phenomena on the pressure distribution is analyzed.

A. Validation

Figure 8 compares the numerical results of the DNS with data from the 3D-PTV measurement series described in Ref. 24. The comparison is shown for nine equidistant cross sections in the x–z plane ranging from $y/d_p = 4$ to $y/d_p = 6.4$. Holes in the experimental plots and areas not covering the full measurement domain are mainly caused by near-wall reflections and limitations in the 3D-PTV evaluation. Figure 8(a) presents the results for $Re_p = 400$. The velocity of the

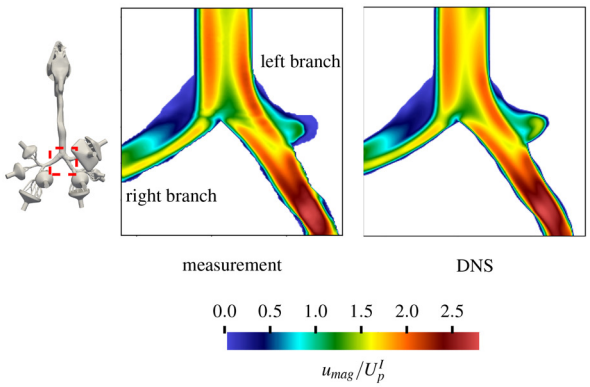

(a) $Re_p = 400$.

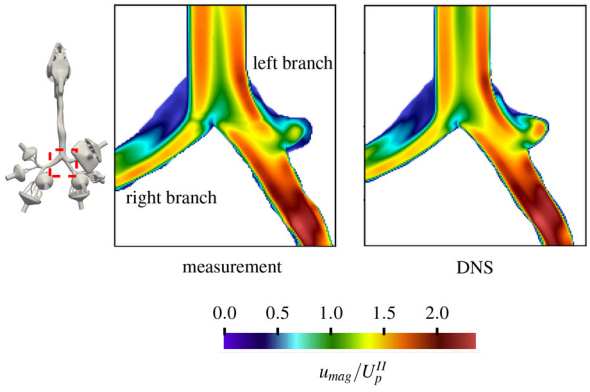

(b) $Re_p = 1200$.

FIG. 9. Contours of the normalized velocity magnitude u_{mag}/U_p in the bifurcation (dashed red square at $z = 0$ in the sketch). Results of the DNS are compared to PIV measurements.[25]

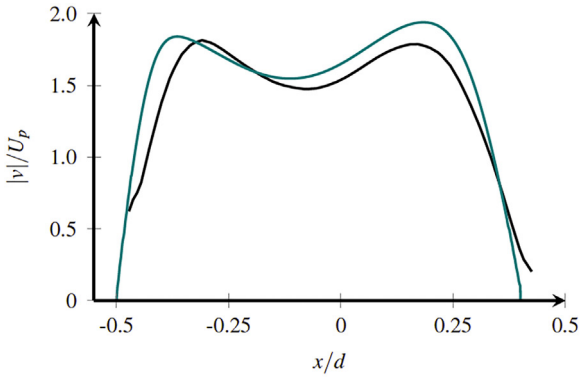

(a) $Re_p = 400$.

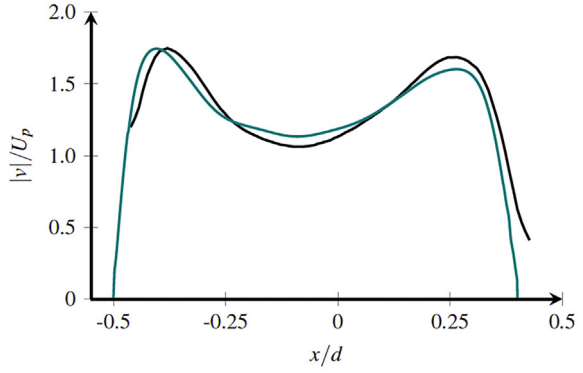

(b) $Re_p = 1200$.

FIG. 10. Profiles of $|v|/U_p$ along the line "CA" (see Fig. 2), in the x-direction at $y/d_p = 0.85$ and $z/d_p = 0.0$ for the DNS (teal) and the PIV measurements from Ref. 25 (black).

high-speed jet in the center agrees well between the simulation and the experiment. Moreover, the DNS accurately reproduces the dented jet shape and the low-velocity region extending into the center across all cross sections. In Fig. 8(b), the numerical results for $Re_p = 1200$ are compared with the 3D-PTV measurements. The slowly flowing region that extends into the center in the first three cross sections is well captured by the DNS, and the high-speed jet also shows very good agreement with the experimental data. Overall, the evolution of the flow structures is consistently well represented by the simulation, demonstrating good agreement between the numerical and experimental results.

Figure 9 compares the flow field at the bifurcation obtained from PIV measurements presented in Ref. 25 with results from the LB simulation in a cross section at $z = 0$ and for $x, y \in [-30\,\text{mm}, 30\,\text{mm}]$. Figure 9(a) shows the comparison for $Re_p = 400$. The measurements reveal two velocity maxima upstream of the bifurcation, a distinct flow separation and a recirculation zone covered by a thin wall jet in the right branch, and two wall jets in the left branch. All of these characteristic flow features are well reproduced by the DNS. For $Re_p = 1200$, shown in Fig. 9(b), the wider wall jet and the smaller recirculation bubble in the right branch, as well as the accelerated flow in the left branch, are captured consistently by both the experiments and the simulations. Overall, the comparison with the experimental data demonstrates that the DNS accurately predicts the flow structures upstream and downstream of the bifurcation.

Figure 10 shows velocity profiles along the line "CA" (see Fig. 2), in the x-direction at $y/d_p = 0.85$ and $z/d_p = 0.0$ for the DNS and PIV measurements from Ref. 25. Considering the optical limitations of the experimental data in the near-wall regions, the overall agreement between the profiles is satisfactory. It is fair to state that the essential flow features are captured by the numerical simulation.

B. Flow structures in the four key anatomical regions

In the following, only results obtained using the fine mesh are discussed. The first key anatomical region is the nasal cavity. Since the time-averaged and instantaneous streamlines at $Re_p = 400$ and $Re_p = 1200$ are quite similar, only the time-averaged streamlines are analyzed. They are shown in Fig. 11 and are colored by the velocity

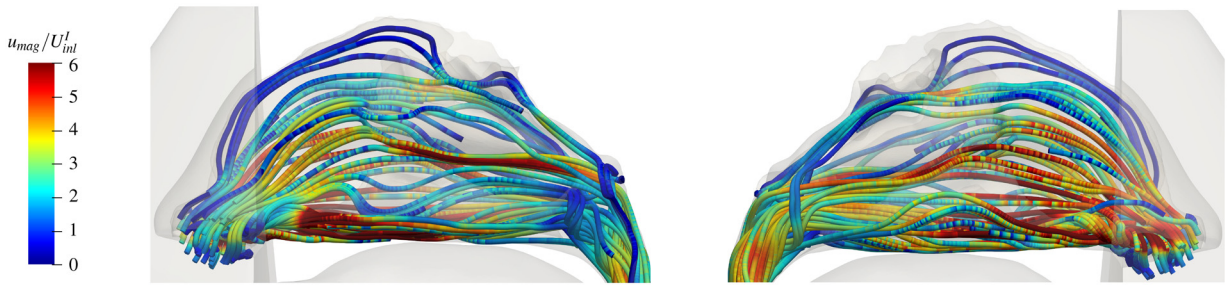

Side view on the left nasal passage

Side view on the right nasal passage

(a) $Re_p = 400$.

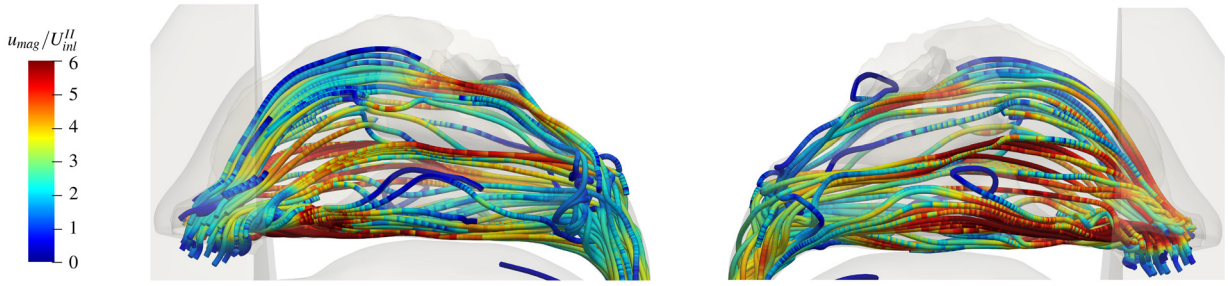

Side view on the left nasal passage

Side view on the right nasal passage

(b) $Re_p = 1200$.

FIG. 11. Streamlines of the time-averaged velocity field in the nasal cavity for $Re_p = 400$ and $Re_p = 1200$ colored by the normalized velocity magnitude u_{mag}/U_{inl}.

magnitude, which is normalized by the inflow velocity. The flow at $Re_p = 1200$ exhibits generally larger normalized velocities compared to the $Re_p = 400$ case. This is especially observed in the channel below the lower turbinate. Other than that, the spatial flow structures are visually only slightly different in the two cases. The flow spreads across all turbinates.

Figure 12 shows u_{mag}/U_{inl} at $Re_p = 400$ and $Re_p = 1200$ in the cross sections I–V, which are defined by the dotted lines in the sketches of the nasal cavity. At both Reynolds numbers, a notable asymmetry is observed between the left and right nasal passages. In the cross sections I–III, the velocity in the right nasal passage is higher than in the left passage. In the cross sections IV and V, the right passage is significantly wider than the left, which leads to a lower velocity and to a more balanced velocity distribution in both nasal passages.

The nasal cavity in this study is not pathological; for instance, a deviated septum is not present. Therefore, it is assumed that the disparity in the cross sections IV and V is likely to be caused by the nasal cycle. The nasal cycle is a natural physiological rhythm during which alternating congestion and decongestion of the turbinates occur in each passage. This leads to a deceleration and acceleration of the flow through the decongested and the congested sides.[75]

The largest difference between the $Re_p = 400$ and $Re_p = 1200$ cases in Fig. 12 is observed in the cross section III. For the higher Reynolds number, increased velocities not only occur near the inferior turbinate but also in the upper channels of the nasal passage. This implies that increased airflow at higher Re numbers enhances the transport of air into the uppermost regions of the nasal cavity, i.e., into the olfactory region. This region contains specialized olfactory epithelium that houses neural receptors responsible for detecting odors.[12] An increased airflow penetration in this area at higher Reynolds numbers is likely to also raise the delivery of odorant molecules to these receptors, which enhances olfactory perception. Such a mechanism is consistent with the physiological role of sniffing, where accelerated airflow and the development of vortical structures improve odor sampling efficiency.

The second key anatomical region covers the nasopharynx and oropharynx. Figure 13 shows streamlines of the time-averaged and instantaneous flow fields in this region, again colored by u_{mag}/U_{inl}. The time-averaged and instantaneous streamlines indicate the development of vortex pairs at $Re_p = 400$ and $Re_p = 1200$. These counter-rotating secondary flow structures are generated in the curved geometry due to centrifugal forces that shift higher-momentum fluid toward the outer bend.[11]

At $Re_p = 400$, the two vortices remain visually well-defined. The higher Reynolds number flow shows vortex pairs that increasingly overlap, especially further downstream, with pronounced differences in the time-averaged and instantaneous streamlines. In the curved section from the nasal cavity to the nasopharynx, the flow accelerates to normalized velocities up to five times higher than U^{I}_{inl}. This enhances secondary vortex formation at both Reynolds numbers. However, at higher Re_p, secondary instabilities are amplified, which increases mixing of the vortical structures when the fluid enters the oropharynx.

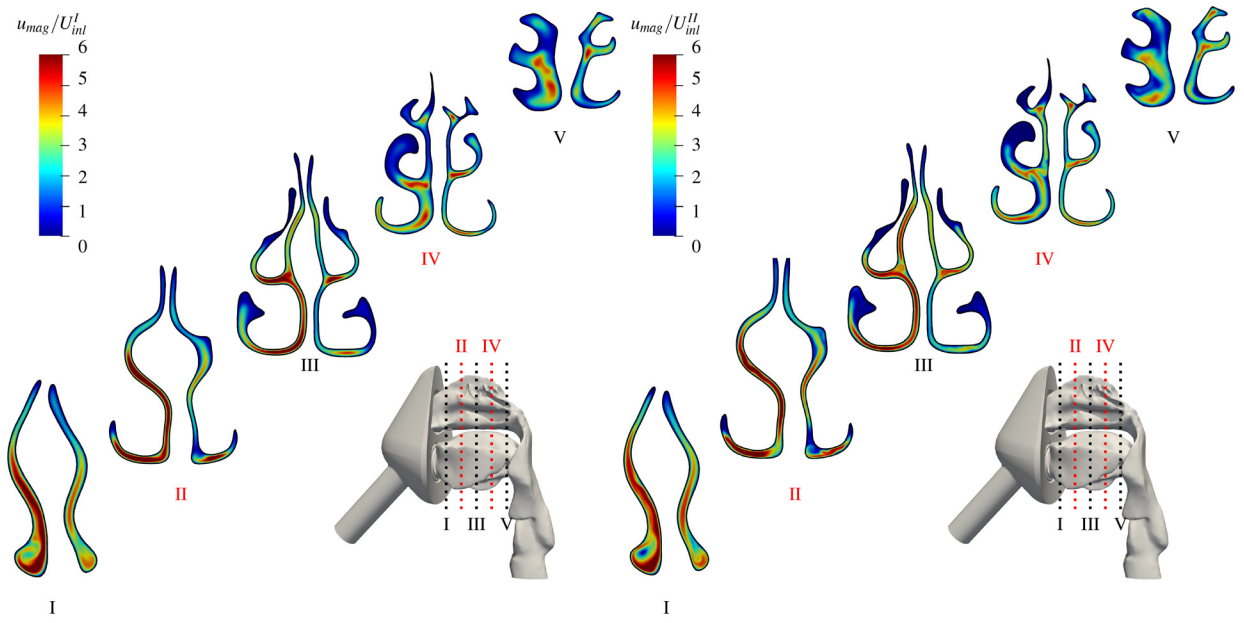

(a) $Re_p = 400$. (b) $Re_p = 1200$.

FIG. 12. Time-averaged normalized velocity magnitude u_{mag}/U_{inl} at $Re_p = 400$ and $Re_p = 1200$ in several cross sections I–V.

Further downstream, the flow decelerates significantly due to the wider cross section which reduces the local strength of the vortices. At $Re_p = 1200$, this emphasizes the difference between the time-averaged and instantaneous streamlines. The latter show a more perturbed behavior that is characteristic of enhanced convective mixing.

This trend is further illustrated in Fig. 14, which shows the time-averaged normalized y-velocity component v in the cross section in the right nasal passage that is illustrated in the sketch. At $Re_p = 400$, the vertical jet remains coherent and expands downward with a relatively high velocity, which indicates limited cross-stream mixing. In contrast, at $Re_p = 1200$, the oropharyngeal jet is wider due to the more intense mixing.

To further investigate the secondary flow structures, the Q-criterion is evaluated for the instantaneous velocity fields at $Re_p = 400$ and $Re_p = 1200$ in Fig. 15. At $Re_p = 400$, coherent and stable vortex structures are clearly identifiable, particularly in the nasopharyngeal region, where the vortex pairs persist over time. These structures are well-defined and remain localized, indicating a laminar flow regime with stable vortical structures. In contrast, at $Re_p = 1200$ the Q-criterion highlights the disintegration of large-scale structures into cascades of smaller, irregular vortices. This breakdown is most prominent in the region downstream of the bend, where the flow decelerates and the mixing is intensified. The loss of coherent vortical structures coincides with a massive growth of fine-scale vortices, resulting in increased spatial complexity and more disordered flow patterns. This observation is consistent with the previously described streamline behavior, where the transition from organized flow in the bend to more chaotic flow in the oropharynx meant enhanced mixing. The generation of small-scale vortical structures in this zone contributes to the dispersive transport of momentum. It emphasizes the role of secondary instabilities in driving mixing at higher Reynolds numbers.

The third key anatomical region is the laryngopharynx and larynx. It contains the glottal jet, which originates at the glottis, i.e., the opening between the vocal folds in the larynx, and which is a key anatomical feature of respiration and phonation. As air passes through this constricted region, it forms a high-velocity core surrounded by pronounced shear layers near the walls. Physiological and *in vitro* studies have extensively characterized this jet. The results emphasize the significant influence of the strong flow acceleration and shear-layer formation on the downstream fluid dynamics.[29,64]

Figure 16 shows the glottal jet at $Re_p = 400$ and $Re_p = 1200$ by time-averaged and instantaneous streamlines. The larger illustrations present the jet from an external perspective, while the smaller illustrations provide an internal view on the symmetry plane of the x axis, highlighting the core of the jet. For $Re_p = 400$, the time-averaged and instantaneous streamlines agree closely. That is, a clear jet core with confined shear layers is evident, especially in the symmetry plane. For $Re_p = 1200$, the jet appears more diffuse and less confined, since the radial momentum is increased, resulting in enhanced mixing. This difference is more evident in the instantaneous streamlines. Nevertheless, it can be stated that unlike in the nasopharynx and oropharynx regions, where time-averaged and instantaneous streamlines deviated significantly at $Re_p = 1200$, they remain similar in the laryngopharynx and larynx region.

The difference between the jets at $Re_p = 400$ and $Re_p = 1200$ becomes more obvious by analyzing the Q-criterion of the instantaneous flow fields in Fig. 17. At $Re_p = 400$, a coherent, high-speed jet

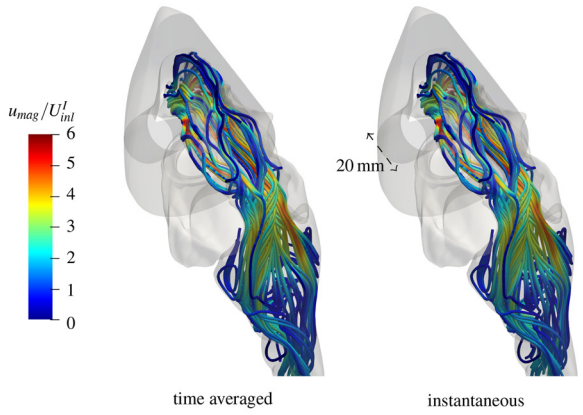

(a) $Re_p = 400$.

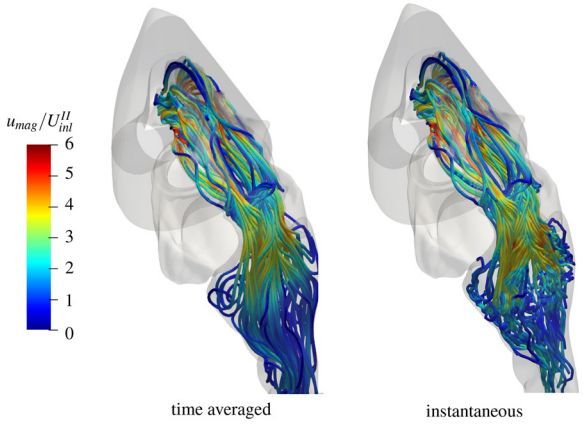

(b) $Re_p = 1200$.

FIG. 13. Streamlines of the time-averaged and instantaneous velocity fields at $Re_p = 400$ and $Re_p = 1200$ colored by the normalized velocity magnitude u_{mag}/U_{inl} in the nasopharynx and oropharynx.

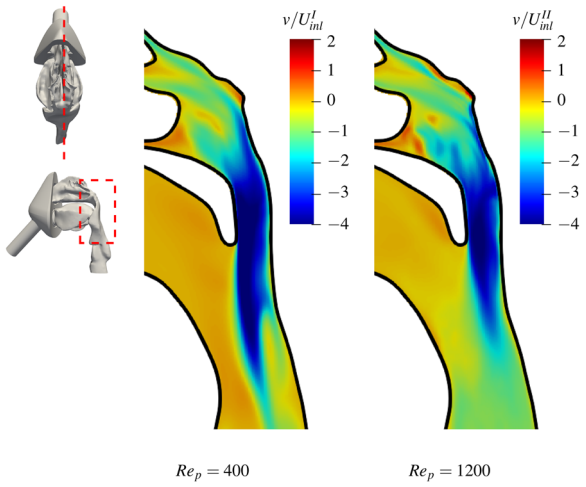

FIG. 14. Time-averaged normalized y-component of the velocity v/U_{inl} at $Re_p = 400$ and $Re_p = 1200$ in a cross section in the right nasal passage (dashed red square and dashed red line in the sketch).

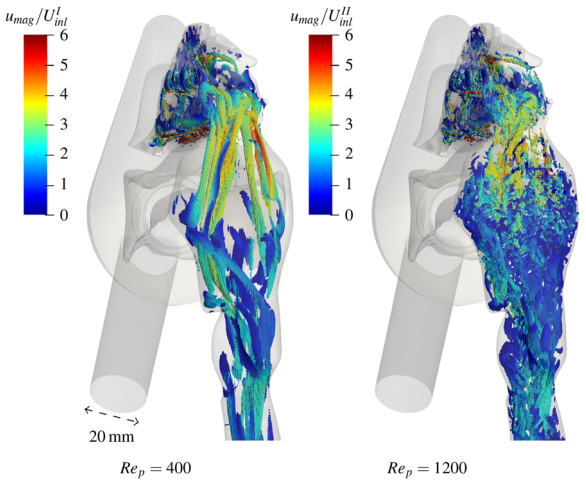

FIG. 15. Q-Criterion of the instantaneous velocity fields at $Re_p = 400$ and $Re_p = 1200$ colored by the normalized velocity magnitude u_{mag}/U_{inl} in the nasopharynx and oropharynx.

core surrounded by shear layers is visible. These shear layers roll up into streamwise vortices, which appear as distinct pairs in the Q-criterion field. This evolution of the shear layer appears to be relatively stable, which is typical for laminar or slightly transitional flows. The Q-distributions for $Re_p = 1200$ show a clear deviation from an organized flow. The shear layers become unstable and develop irregular vortical structures. This indicates a highly unsteady flow, which is characterized by complex vortex interactions. The transition from symmetric to disordered, multiscale vortices evidences the sensitivity of the structure of the glottal jet to the Reynolds number and the increased mixing and shear-layer thickening at higher flow rates.

Further investigation of the distribution of high-speed regions along the airway centerline reveals that for both Reynolds numbers u_{mag} exceeds $4U_{inl}$. This is primarily true within the nasal cavity and the nasopharyngeal region in Figs. 11 and 13. These regions act as geometric constrictions that locally accelerate the flow, particularly near the curved transitions and narrow passages. Such geometric constrictions, e.g., caused by the nasal turbinates and valve regions, are crucial for heat and moisture exchange and thereby enhance mucosal contact with inhaled air.[81] Temperature increase and humidification in the nasal cavity are strongly correlated and happen almost synchronously.[27] However, narrow nasal passages also increase the airway resistance. To improve the breathing conditions by, e.g., nasal cavity surgeries, a compromise between reducing the pressure loss by widening and better conditioning the incoming air before entering the lung by narrowing the airway has to be found.[50,52,54] In contrast to the nasal cavity or nasopharynx, in regions downstream from the oropharynx to the glottal jet, lower peak velocities are observed, with local velocity magnitude values generally remaining below $4U_{inl}$ (Figs. 16 and 17).

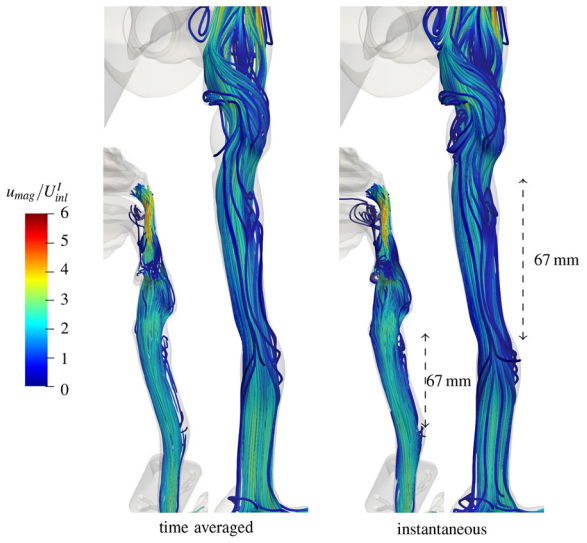

(a) $Re_p = 400$.

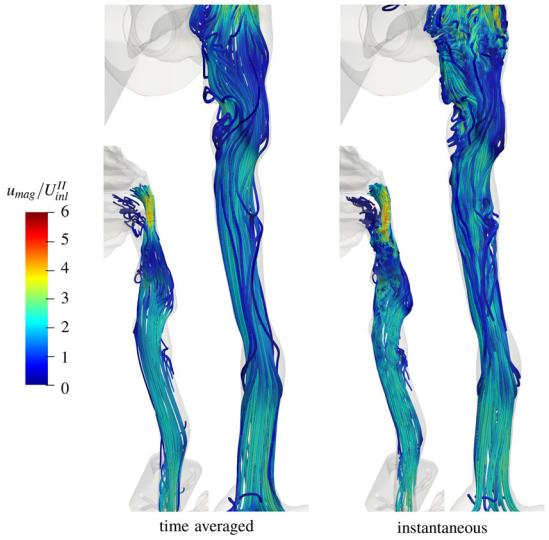

(b) $Re_p = 1200$.

FIG. 16. Streamlines of the time-averaged and instantaneous velocity fields at $Re_p = 400$ and $Re_p = 1200$ colored by the normalized velocity magnitude u_{mag}/U_{inl} in the laryngopharynx and larynx. For each case, the larger illustration presents the jet streamlines from an external perspective, while the smaller illustration provides an internal view with streamlines clipped in the symmetry plane of the x axis, showing the core of the jet.

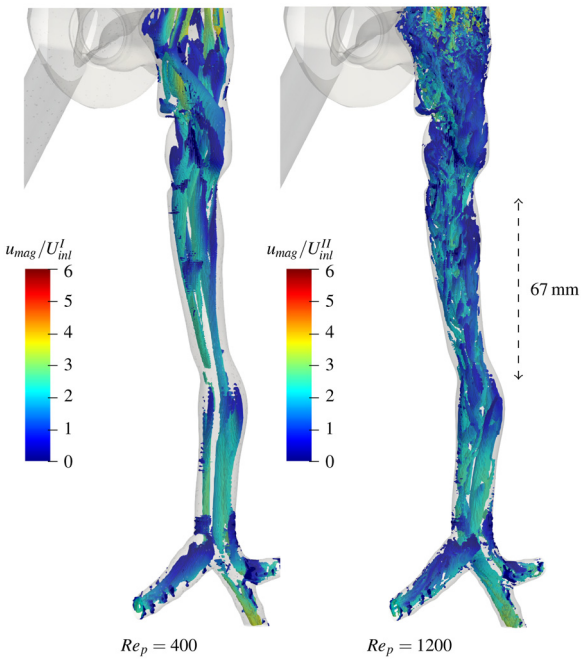

FIG. 17. Q-Criterion of the instantaneous velocity fields at $Re_p = 400$ and $Re_p = 1200$ colored by the normalized velocity magnitude u_{mag}/U_{inl} in the laryngopharynx and larynx.

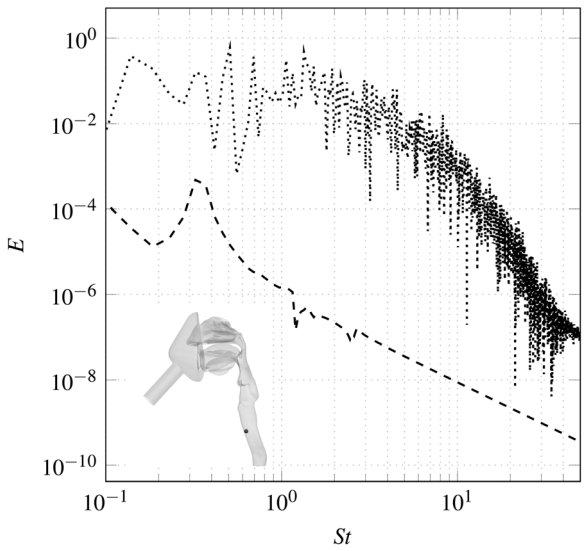

FIG. 18. Velocity energy spectra in the shear layers of the glottal jet at the location illustrated by the dot at $Re_p = 400$ (dashed) and $Re_p = 1200$ (dotted).

This decrease correlates with the anatomical widening of the airway, which results in flow deceleration and redistribution.

To complement the spatial analysis of the glottal jet and gain insight into the temporal dynamics of the shear layers, the energy spectrum of the velocity fluctuations at a probe point located within the shear region of the jet is evaluated in Fig. 18. While the Q-criterion provides a snapshot of vortical structures at a given time, the energy spectrum captures the frequency content of the flow over time. This allows the assessment of the presence of coherent structures, dominant oscillatory modes, and broadband turbulence. In particular, the comparison of the spectra at $Re_p = 400$ and $Re_p = 1200$ yields a

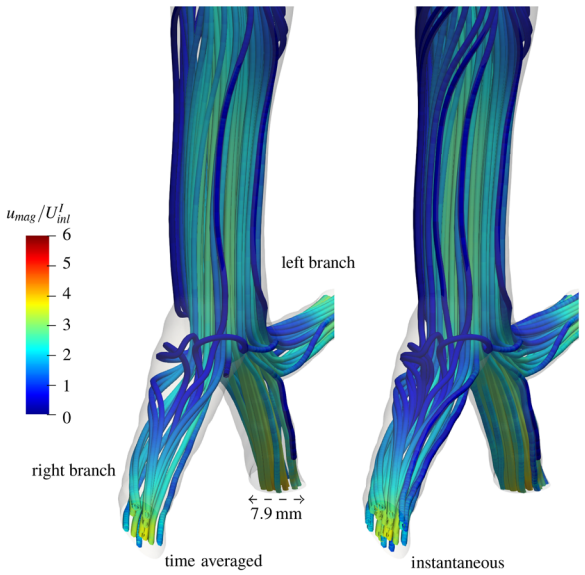

(a) $Re_p = 400$.

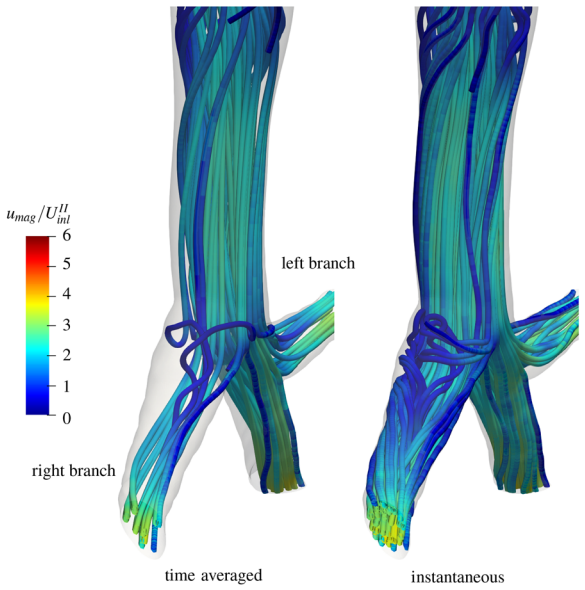

(b) $Re_p = 1200$.

FIG. 19. Streamlines of the time-averaged and instantaneous velocity fields for $Re_p = 400$ and $Re_p = 1200$ colored by the normalized velocity magnitude u_{mag}/U_{inl} in the tracheal and post-carinal regions.

quantitative measure of how the shear-layer dynamics evolve from organized vortex roll-up to increasingly irregular, multi-frequency interactions.

At $Re_p = 400$, the energy spectrum exhibits a clear peak at approximately $St = 0.35$. This indicates the presence of the dominant large-scale, quasi-periodic structure, which is likely associated with

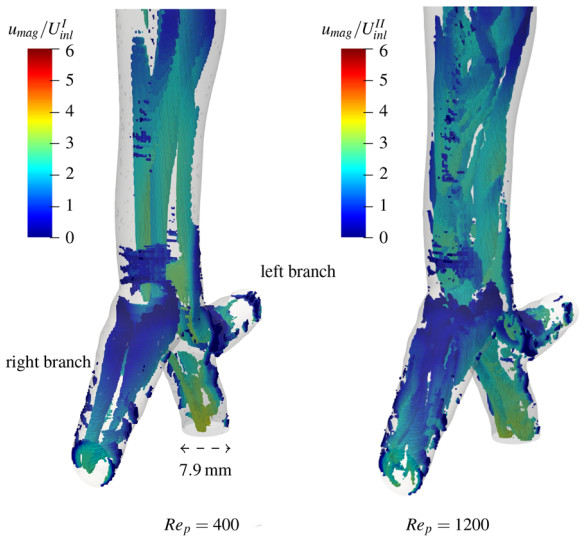

FIG. 20. Q-Criterion of the instantaneous velocity fields at $Re_p = 400$ and $Re_p = 1200$ colored by the normalized velocity magnitude u_{mag}/U_{inl} in the tracheal and post-carinal regions.

coherent shear-layer dynamics. Beyond this peak, the spectrum shows an almost linear decay in log–log space. This suggests that the flow remains largely organized with only limited energy transfer to smaller turbulent scales.

For $Re_p = 1200$, the spectrum reveals a more complex multi-regime structure. A low-frequency range below $St = 2$ captures the energy containing eddies and large-scale flow instabilities. This is followed by a well-defined intermediate region ranging from $St = 2$ to $St = 10$. In this regime, the energy is transferred from larger to smaller scales without significant loss. At frequencies higher than $St = 10$, the spectrum enters a dissipation range, where the energy content decays rapidly due to viscous effects.

The final key anatomical region contains the trachea, the carinal bifurcation, and the post-carinal region. As can be seen in Fig. 19, the time-averaged and instantaneous streamlines at $Re_p = 400$ and $Re_p = 1200$ are largely aligned, indicating limited temporal variability and a relatively stable flow regime. This result is similar to the glottal jet region. However, a key distinction emerges in the tracheal jet upstream of the carinal bifurcation. At $Re_p = 400$, the jet remains well-defined with clearly visible shear layers surrounding the high-speed core. In contrast, at $Re_p = 1200$ the jet is again more diffuse with broadened shear zones and reduced central velocity. Again, this is due to enhanced momentum exchange and mixing upstream of the bifurcation.

Downstream of the bifurcation, these differences are less pronounced. As discussed in Sec. III A, Figs. 9(a) and 9(b) show a clear flow separation region and thin wall jet in the right branch and a much smaller separation region with two wall jets that merge into one jet downstream in the left branch. In the right branch, the flow patterns for both Reynolds numbers are characterized by separation and vortex pairs, which differ quantitatively. Overall, the geometry-induced secondary flows dominate the post-bifurcation dynamics and impose a consistent structure on the downstream flow despite the upstream variations in the jet structure and turbulence intensity.

When the high-speed tracheal jet impinges upon the carinal bifurcation, it is divided into ducts with a smaller cross-sectional area relative to the wide glottal region. However, the cumulative cross-sectional area of the daughter branches exceeds that of the tracheal inlet, resulting in an overall reduction in momentum and convective acceleration. This overall geometric expansion combined with the redistribution of the flow into curved ducts reduces asymmetries from the upstream flow. This flow-stabilizing effect is observed for both REYNOLDS number flows.

This discussion is further supported by an analysis of the Q-criterion distributions of the instantaneous velocity field in Fig. 20. For both REYNOLDS numbers, vortex pairs determine the flow in the bifurcated branches, which leads to increased mixing and, as such, to a uniform velocity distribution further downstream.

Finally, the flow-stabilizing role of the carinal bifurcation is underlined by examining the recirculation region downstream of the carinal bifurcation. Figure 21 shows the time-averaged velocity vectors for $Re_p = 400$ and $Re_p = 1200$ as spatially scaled arrows colored by u_{mag}/U_{inl}. The arrows originate from cross sections in the tracheal and post-carinal regions, which are also colored by u_{mag}/U_{inl}. For both REYNOLDS numbers, the vector fields exhibit nearly identical patterns. Upstream, the two local velocity maxima described earlier in this study are clearly visible. Downstream of the bifurcation, the flow reattaches in the fourth cross-sectional area along the right branch, while in the left branch the recirculation region extends into the second cross-sectional area of the secondary bifurcation's left branch. Interestingly, the size of the recirculation regions and the reattachment locations appear largely independent of the REYNOLDS number. This behavior can partly be attributed to the slight narrowing of the daughter branches, which promotes a local acceleration of the flow and enforces reattachment of the separated shear layers. Overall, the consistent reattachment behavior across both REYNOLDS numbers reinforces the conclusion that the carinal bifurcation exerts a stabilizing influence on the downstream flow.

C. Pressure loss along the four key anatomical regions

The previously described flow features at the two REYNOLDS numbers affect the pressure drop, a key quantity in respiratory flows. Elevated pressure loss along the airway increases the load on the respiratory muscles and can lead to reduced ventilation efficiency.[33,40] The pressure drop is extracted from the simulation results using the reference quantities for air, denoted in Table I. The distribution of the time-averaged total pressure is determined along the geometrical centerline between the characteristic locations S_1 (right nostril) and S_7/S_8 (post-carinal region). Figure 22 shows the distributions of the total pressure loss $\Delta p_{tot}(s) = \hat{p}_{tot}(S_1) - \hat{p}_{tot}(s)$ for both REYNOLDS numbers, where $\hat{p}_{tot}(S_1)$ is the area-averaged total pressure in the cross section of S_1 and $\hat{p}_{tot}(s)$ is the area-averaged total pressure at the downstream cross section at location s along the centerline.

The pressure loss distributions between the right nostril (S_1) and seven characteristic points $S_2, \ldots, S_8$ along the centerline are analyzed. The total pressure loss between S_1 and S_7 in the left post-carinal branch is $\Delta p_{tot}(S_7) = 9.76$ Pa for $Re_p = 400$ and $\Delta p_{tot}(S_7) = 41.93$ Pa for $Re_p = 1200$. That is, the latter is 4.3 times larger than the former. The contributions of each key anatomical region to $\Delta p_{tot}(S_7)$ are listed in Tables II and III. For both REYNOLDS numbers, the largest contributions occur in the nasal cavity between S_1 and S_2.

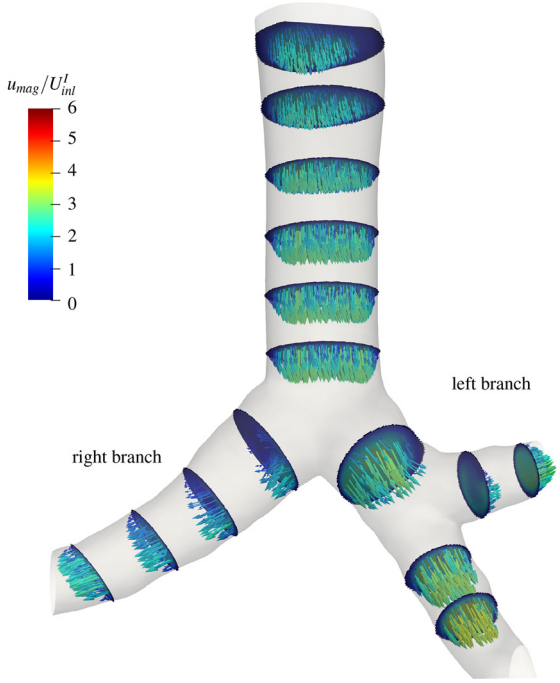

(a) $Re_p = 400$.

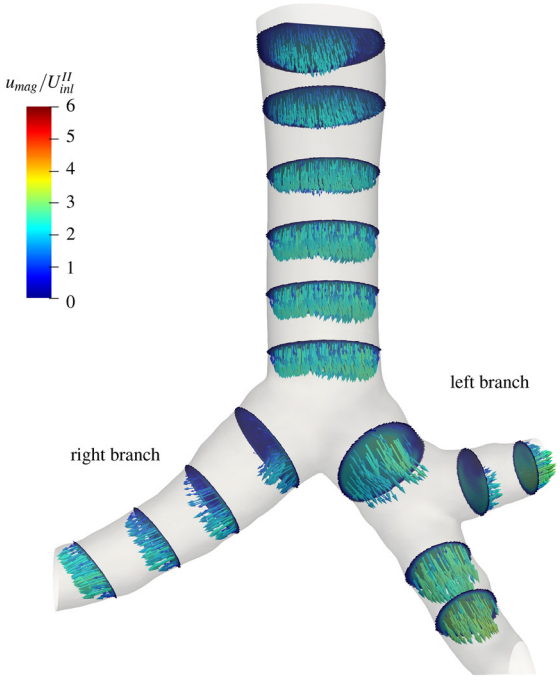

(b) $Re_p = 1200$.

FIG. 21. Time-averaged velocity vectors for $Re_p = 400$ and $Re_p = 1200$, shown as spatially scaled arrows colored by the normalized velocity magnitude u_{mag}/U_{inl}. The arrows originate from cross sections in the tracheal and post-carinal regions, which are also colored by u_{mag}/U_{inl}.

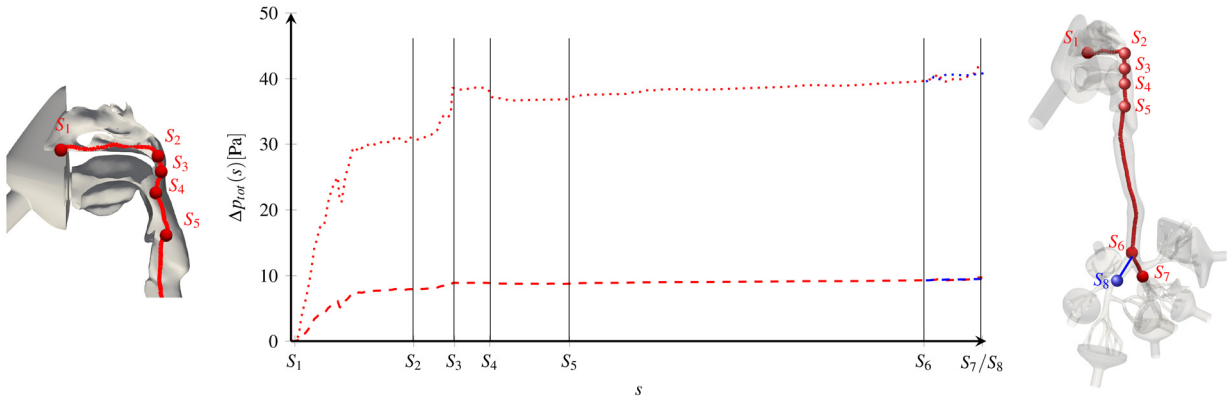

FIG. 22. Total pressure loss between the right nostril and several locations along the airway beyond the carinal bifurcation for the $Re_p = 400$ (dashed) and $Re_p = 1200$ (dotted) cases. The various locations are indicated in the 3D models. The distributions between S_6 and S_7/S_6 and S_8 are shown by red/blue lines.

The pressure drop is caused by the narrow nasal valve region and the complex internal geometry defined by curved walls and turbinates. These geometric features cause the local flow to separate and enhance viscous dissipation. This is consistent with the velocity field observations presented in Sec. III B. Although the streamline fields look similar for both Reynolds numbers, the higher normalized velocities at $Re_p = 1200$, especially around the turbinates, mean higher kinetic energy and thus increased dynamic pressure. The kink midway between S_1 and S_2 occurs due to the widening between cross sections III and IV in Fig. 12, which has been discussed in Sec. III B.

The second largest difference in the pressure loss for $Re_p = 400$ and $Re_p = 1200$ is observed in the naso- and oropharyngeal regions between S_2 and S_5. The pressure loss Δp_{tot} increases by 0.86 Pa for $Re_p = 400$ and by 6.23 Pa for $Re_p = 1200$. This increase is mainly due to the nasopharyngeal bend by which the flow is directed sharply downward. At $Re_p = 400$, the flow remains laminar, and the centrifugal forces generate vortex pairs, as shown in Fig. 13(a). In this laminar flow, momentum is efficiently redistributed with limited energy dissipation, leading to only a mild pressure drop. At $Re_p = 1200$, however, the vortices disintegrate into a cascade of smaller vortical structures, as evidenced by the Q-criterion analysis in Fig. 15. This breakdown of coherent motion and the development of fine-scale flow features enhances viscous dissipation and mixing and significantly increases the total pressure loss. A nearly constant pressure loss is observed in the narrow part of the oropharyngeal region between S_3 and S_4 regardless of the Reynolds number. An expansion of the airway in the widened part of the oropharyngeal region between S_4 and S_5 reduces the pressure loss slightly in both flow regimes.

A further pressure loss increase is observed in the laryngopharynx and larynx, i.e., the region of the glottis jet between S_5 and S_6. At $Re_p = 400$, Δp_{tot} increases by 0.53 Pa and by 2.57 Pa for $Re_p = 1200$. The gradient of the total pressure loss between S_5 and S_6 is small compared to that of the nasal cavity and nasopharyngeal bend for both Reynolds numbers. This can be attributed to the distinct flow dynamics of the glottal jet. While this region features high local velocities due to the constricted glottis, the jet is highly directed and essentially independent from strong wall interactions in its core. At $Re_p = 400$, the jet retains a coherent laminar structure with symmetric shear layers, resulting in limited energy dissipation and thus a small total pressure drop of less than 1 Pa. At $Re_p = 1200$, the total pressure loss is at a much higher level. The jet is more diffuse, and the shear layers break down into smaller vortices, as evidenced by the Q-criterion and energy spectrum in Figs. 17 and 18, which leads to enhanced mixing and the higher pressure loss level. The geometric confinement of the glottis primarily accelerates the flow without inducing significant frictional losses along the airway wall such that the overall pressure gradient remains moderate.

TABLE II. Contributions of the four key anatomical regions to the total pressure loss for flow at $Re_p = 400$.

Key anatomical region	Points along centerline	Change in Δp_{tot} (Pa)	Contribution to Δp_{tot} (S_7) (%)
Nasal cavity	S_1–S_2	+7.93	81.25
Naso- and oropharynx	S_2–S_5	+0.86	8.81
Laryngopharynx and larynx	S_5–S_6	+0.53	5.43
Trachea and left car. branch	S_6–S_7	+0.44	4.51
Trachea and right car. branch	S_6–S_8	+0.23	⋯

TABLE III. Contributions of the four key anatomical regions to the total pressure loss for flow at $Re_p = 1200$.

Key anatomical region	Points along centerline	Change in Δp_{tot} (Pa)	Contribution to Δp_{tot} (S_7) (%)
Nasal cavity	S_1–S_2	+30.76	73.36
Naso- and oropharynx	S_2–S_5	+6.23	14.86
Laryngopharynx and larynx	S_5–S_6	+2.57	6.13
Trachea and left car. branch	S_6–S_7	+2.37	5.65
Trachea and right car. branch	S_6–S_8	+1.19	⋯

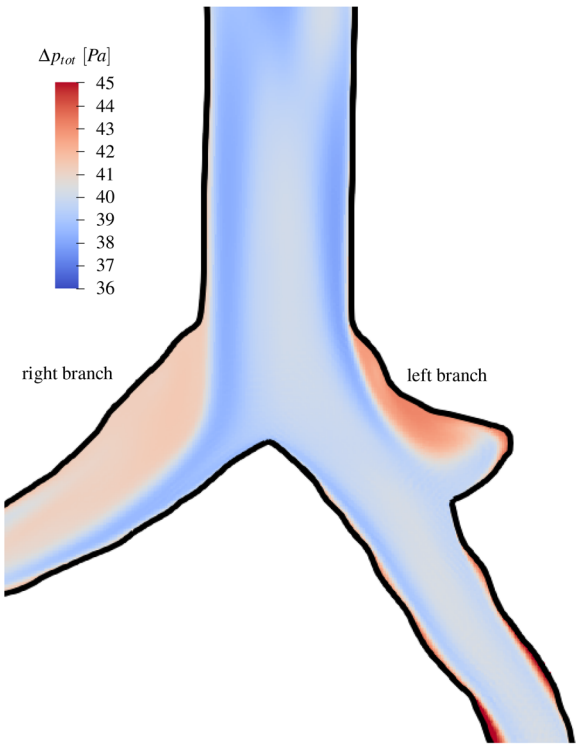

FIG. 23. Total pressure loss between the right nostril and the carinal bifurcation region for $Re_p = 1200$. The location of the cross section is shown in the sketch of Fig. 6.

In the final key anatomical region, the total pressure loss between the trachea (S_6) and the left (S_7) and right (S_8) branches of the carinal bifurcation are analyzed. Between S_6 and S_7, the pressure loss increases moderately by 2.37 Pa at $Re_p = 1200$, whereas almost no increase is observed at $Re_p = 400$. At $Re_p = 400$, the jet remains focused and coherent with minimal shear-induced dissipation, leading to a negligible pressure drop in this segment. In contrast, at $Re_p = 1200$, the jet is already more diffuse upstream of the bifurcation, see Fig. 19(b), and the enhanced mixing within its broadened shear layers contributes to increased viscous losses as the flow transitions into the left daughter branch.

Similar to the difference between S_6 and S_7, almost no increase in the total pressure is observed between S_6 and S_8 for $Re_p = 400$. For $Re_p = 1200$, the increase is 1.19 Pa. That is, it is smaller than the increase between S_6 and S_7. Despite the larger recirculation zone in the right branch, as shown in Fig. 9(b), Fig. 23 indicates that the left branch exhibits a greater total pressure loss. The increased loss in the left branch is caused by another bifurcation shortly downstream of the carinal bifurcation. This introduces additional curvature, branching, and cross-sectional variation by which secondary flow structures are intensified. They are additional sources of energy dissipation, particularly at the higher Reynolds number.

Nonetheless, the overall pressure loss remains modest compared to upstream regions. This is likely due to the flow-stabilizing effect of the carinal bifurcation, which has been discussed in Sec. III B. The cumulative cross-sectional area of the daughter branches exceeds that of the tracheal inlet, resulting in an overall reduction in flow velocity and thus, in momentum and convective acceleration.

The relative contribution of the nasal cavity to the total pressure loss is with 81.25% at $Re_p = 400$ larger than 73.36% at $Re_p = 1200$. Interestingly, this is reversed for the naso- and oropharynx with 8.81% at $Re_p = 400$ and 14.86% at $Re_p = 1200$, the laryngopharynx and larynx with 5.43% at $Re_p = 400$ and 6.13% at $Re_p = 1200$, and the trachea and carinal bifurcation with 4.51% and 5.65% at $Re_p = 400$ and $Re_p = 1200$.

IV. SUMMARY, DISCUSSION, AND OUTLOOK

Fully resolved, turbulence-model-free simulations of respiratory flows through a realistic human upper airway geometry at two physiologically relevant Reynolds numbers are presented. Previous numerical studies frequently relied on simplified geometries or were based on the RANS equations plus a closure model such that the accuracy was limited, among other constraints, by modeling assumptions. To reduce the modeling impact, DNS of nasal breathing in an airway model from a nasal mask to the sixth bronchial bifurcation was conducted. The simulations were performed at $Re_p = 400$ and $Re_p = 1200$, representing resting and moderately elevated breathing conditions. A high-fidelity LB method implemented in the open-source framework m-AIA was validated against high-resolution PIV and 3D-PTV measurements.

A comprehensive mesh refinement study was conducted to evaluate the impact of the spatial resolution on the accuracy of the numerical simulations. The coarse simulation underpredicted the jet core velocity and failed to resolve key flow structures observed in the measurements. The medium and fine meshes reproduced the spatial development of the jet for both Reynolds numbers. The fine mesh yielded the best agreement with the experimental data in velocity magnitude and flow structure. Therefore, the fine mesh was used for all subsequent analyses.

The flow field in four key anatomical regions of the airway was investigated: the nasal cavity, the naso- and oropharynx, the laryngopharynx and larynx (glottal jet region), and the trachea with the carinal bifurcation. In the following, the major findings of this investigation are summarized.

- **Nasal cavity**: The nasal cavity exhibited the most significant total pressure loss in the entire airway, particularly at $Re_p = 1200$, where Δp_{tot} reached approximately 30.76 Pa compared to 7.93 Pa at $Re_p = 400$. This is attributed to the narrow nasal valve and the complex internal geometry defined by the turbinates such that the flow is locally accelerated and vortices are generated. The analysis of the velocity field showed high-speed flow in the inferior and center turbinate channels. The streamline patterns remained similar between both Reynolds number flows. The asymmetry between the left and right passages, which is likely linked to the nasal cycle, contributed to uneven pressure and velocity distributions that amplified local losses. At $Re_p = 1200$, higher airflow into the uppermost part of the nasal cavity sensitized the neural receptors in the olfactory region.
- **Nasopharynx and oropharynx**: The second notable total pressure loss occurred in the naso- and oropharyngeal regions, with Δp_{tot} increasing by 6.23 Pa at $Re_p = 1200$ and 0.86 Pa at $Re_p = 400$. At the lower Reynolds number, secondary vortices were stable, resulting in a structured but low-dissipation flow. At

$Re_p = 1200$, vortices disintegrated into chaotic interactions and enhanced mixing. This increased dissipation led to higher total pressure loss. Further downstream, in the widened part of the oropharynx, the total pressure loss even slightly decreased.

- **Laryngopharynx and larynx**: In the glottal region, a further rise in the total pressure loss due to the different strength of the shear layers coating the jet was observed, i.e., 2.57 Pa at $Re_p = 1200$ and less than 1 Pa at $Re_p = 400$. In general, the glottis acts as a geometric nozzle that channels the flow and limits the overall pressure drop relative to more constricted upstream regions.
- **Trachea and carinal bifurcation**: This segment showed a moderate pressure rise of 2.37 Pa for $Re_p = 1200$ and hardly any changing pressure at $Re_p = 400$ for the flow from the trachea into the left branch downstream of the bifurcation. Similarly, for the flow into the right branch, almost no change in pressure was observed at $Re_p = 400$. However, the pressure difference of 1.19 Pa for $Re_p = 1200$ was smaller than in the left branch. The increased total pressure loss in the left branch comes mainly from another bifurcation shortly downstream of the main carinal bifurcation. Nevertheless, the overall pressure loss remained modest compared to upstream regions. When the tracheal jet reaches the carinal bifurcation, it splits into narrower but cumulatively wider daughter branches, leading to reduced momentum and convective acceleration.

The present findings showed that the nasal cavity plays a key role in olfactory transport. Under normal resting conditions, only a small fraction of the inhaled air (5%–15%) reaches the olfactory region. Most of the flow bypasses it along the lower part of the nasal cavity.[28] At higher Reynolds numbers, an increased flow penetration into the superior nasal regions was observed. This corroborates the conclusions by Zhao *et al.*[79] and Kelly *et al.*,[28] who found that enhanced airflow toward the olfactory system improves sensory perception during sniffing. The results of the current study clearly agree with this interpretation and provide further confirmation by cross-sectional velocity field data.

The transition from stable secondary vortices at $Re_p = 400$ to chaotic secondary flows at $Re_p = 1200$ in the naso- and oropharyngeal regions leads to enhanced convective mixing. On the one hand, stronger mixing promotes more uniform heat and humidity exchange. On the other hand, higher mixing also increases wall contact and residence times for inhaled particles and droplets, resulting in adverse implications for the following:

- Pathogen transmission: Turbulent eddies can carry infectious aerosols toward the mucosal surface, facilitating viral uptake.[4]
- Mucosal irritation: Inhalation of pollutants or irritants is more likely to result in contact with sensitive pharyngeal tissue.
- Uncontrolled drug deposition: For inhalation therapies targeting the lower airways, excessive upstream mixing increases the risk of premature deposition in the pharynx, which might reduce the therapeutic dose reaching distal regions.[78]

These effects should be considered in the design of aerosol-based treatments and surgical interventions that alter pharyngeal geometry.

Regarding the glottal jet, at the lower Reynolds number, the jet had a focused core with coherent shear layers and symmetric roll-up into streamwise vortices. In contrast, the higher Reynolds number case showed widened shear layers and shear-layer breakdown that generated turbulence. Similar patterns have been reported in laboratory models. At higher Reynolds numbers, the glottal flow changes from laminar-like jets to turbulent shear layers that enhance mixing and shear-induced energy dissipation.[64] For aerosol therapies targeting lower airways, the glottal transition influences aerosol trajectory and dispersion. Higher turbulence may improve downstream penetration but also increases the deposition likelihood at the vocal fold region, potentially exposing the local tissue to irritants or drugs.

The strong jet and shear layers in the glottal region are related to aerodynamic sound generation mechanisms.[43] In phonation, periodic flow separation and shear-layer roll-up downstream of the glottis act as acoustic sources. Even without explicitly simulating vocal fold vibration, the present simulations suggest that the jet deflection and free shear layers observed at the higher Reynolds number can act as potential sound sources.[70]

A novel and central contribution of the present study is the systematic discussion of the pressure loss in four anatomically distinct regions of the airway. This multi-regional analysis revealed that pressure loss is not only a passive by-product of airway resistance but also a sensitive marker for the transition from laminar flow to multiscale dynamics. Interestingly, while the nasal cavity accounts for the largest share of the absolute pressure loss at both flow rates, its relative contribution decreases from over 80% at $Re_p = 400$ to about 73% at $Re_p = 1200$. This indicates that downstream regions contribute more significantly at higher flow rates.

The observed distribution of pressure losses across the airway has direct physiological significance. The nasal cavity, which accounts for the majority of the total pressure drop, nearly determines the overall resistance during nasal inspiration. Increased pressure losses in this region imply a greater inspiratory effort and may thus play a role in breathing discomfort or obstructive conditions, such as nasal valve collapse.[20]

Beyond the specific flow analyses, an important outcome of this study is the establishment of a comprehensive benchmark for respiratory flow in a realistic airway geometry. Previous studies have primarily focused on idealized airway segments, e.g., a DNS of flow through a symmetric bifurcation model with a prescribed centered inflow jet,[68] or an LES of flow through a simplified asymmetric bifurcation with a uniform inlet velocity[41] have been performed. While such configurations might be useful for specific flow investigations, they do not reproduce the complex upstream–downstream coupling that characterizes realistic flow through the carinal bifurcation, since the velocity profiles in Fig. 10 clearly show a jet with two local maxima upstream of the carinal bifurcation. This inherently asymmetric inflow gives rise to distinct flow separation and reattachment patterns in the daughter branches, which cannot be captured by isolated or idealized bifurcation models. Further similar studies focus on specific breathing conditions; e.g., in Ref. 6, an LES of sniffing with fundamentally different flow physics was performed. Together with the accompanying experimental validation, the presented DNS results provide fully resolved, turbulence-model-free data that capture the complete spectrum of spatial and temporal flow scales, including transitional and secondary flow phenomena.

Despite these advances, several limitations exist in the present study. First, the simulations represent a steady-state inhalation. Therefore, they do not capture the temporal variations during a full breathing cycle. Extending the analysis to unsteady, time-resolved

inhalation and exhalation would provide additional insight into cyclic flow development and hysteresis effects. Second, only nasal breathing was considered. Oral or combined nasal–oral breathing modes, which can dominate at higher flow rates or under pathological conditions, were not addressed. Third, the investigation is based on a single subject-specific geometry, which limits the generality of the findings. However, interindividual anatomical variability can substantially influence flow partitioning and pressure losses. Fourth, fluid–structure interaction effects, such as wall motion or compliance of soft tissues in the pharyngeal and laryngeal regions, were neglected. These may play an important role in realistic airflow dynamics and sound generation. Fifth, the range of simulated REYNOLDS numbers was restricted to two representative inspiratory conditions. Higher flow intensities or pathological airflow regimes may exhibit additional transitional or turbulent features not captured here. Finally, the simulations did not account for the presence of the mucus layer that covers the nasal and airway walls. This layer can locally alter wall roughness, effective geometry, and near-wall flow behavior, thereby influencing shear stresses, heat and mass transfer, and potentially particle deposition.

The present simulations establish a high-fidelity reference for future investigations that incorporate comparisons between nasal and oral breathing modes as well as simulations and measurements covering complete breathing cycles. The investigations aim to provide an even more comprehensive understanding of patient-specific airflow patterns and to support the design of optimized inhalation therapies and surgical interventions tailored to individual anatomies.

ACKNOWLEDGMENTS

The research leading to these results has been funded by the German Research Foundation within the Walter Benjamin fellowship RU 2771/1-1 and by the HANAMI project within the European Union Horizon Europe Programme—Grant Agreement No. 101136269 under the call HORIZON-EUROHPC-JU-2022-INCO-04. The authors gratefully acknowledge computing time on the supercomputer JURECA-DC[69] at Forschungszentrum Jülich under Grant No. *jhpc54*. The authors are grateful to Dr. František Lízal and his team at the Brno University of Technology for providing the three-dimensional digital model geometry of the respiratory tract.

AUTHOR DECLARATIONS

Conflict of Interest

The authors have no conflicts to disclose.

Author Contributions

Mario Rüttgers: Conceptualization (lead); Formal analysis (lead); Funding acquisition (lead); Investigation (lead); Methodology (lead); Project administration (lead); Software (lead); Supervision (lead); Validation (lead); Visualization (lead); Writing – original draft (lead); Writing – review & editing (equal). **Julian Vorspohl:** Conceptualization (lead); Formal analysis (lead); Investigation (lead); Methodology (lead); Software (equal); Validation (lead); Visualization (lead); Writing – original draft (lead); Writing – review & editing (equal). **Luca Mayolle:** Data curation (supporting); Methodology (supporting). **Benedikt Johanning-Meiners:** Data curation (lead); Methodology (lead); Writing – original draft (lead). **Dominik Krug:** Supervision (supporting). **Michael Klaas:** Funding acquisition (supporting). **Matthias Meinke:** Funding acquisition (supporting); Software (supporting). **Sangseung Lee:** Supervision (supporting). **Wolfgang Schröder:** Funding acquisition (equal); Supervision (equal); Writing – original draft (equal). **Andreas Lintermann:** Conceptualization (equal); Formal analysis (supporting); Funding acquisition (lead); Investigation (supporting); Methodology (equal); Project administration (lead); Resources (lead); Software (equal); Supervision (lead); Validation (supporting); Writing – review & editing (equal).

DATA AVAILABILITY

The data that support the findings of this study are available from the corresponding author upon reasonable request.

NOMENCLATURE

A_{inl}	Cross-sectional area at the inlet
A_p	Cross-sectional area at the pharynx
C_p	Circumference of A_p
c_s	Isothermal speed of sound
d_{inl}	Inlet diameter
d_{outl}	Outlet diameters
d_p	Hydraulic diameter at the pharynx
E	Spectral energy
f	Particle probability distribution function
fr	Temporal frequency
L_e	Minimum entrance length of the inlet pipe in the experiments
L_{inl}	Length of the inlet pipe in the experiments
n	Refractive index
p_{dyn}	Dynamic pressure
p_{stat}	Static pressure
p_{tot}	Total pressure
p_0	Reference pressure
Q	Q-criterion
Re	Reynolds number
Re_{inl}	Reynolds number at the inlet
Re_p	Reynolds number at the pharynx
St	Strouhal number
Sto	Stokes number
s	Point along the centerline
t	Time
U_{inl}	Spatially averaged velocity at the inlet
U_p	Spatially averaged velocity at the pharynx
u	Velocity component in the x-direction
u_{mag}	Velocity magnitude
v	Velocity component in the y-direction
w	Velocity component in the z-direction
wc_i	Weight coefficients
α	Inclination angle of the inflow pipe
Δx	Cell size
δ	Wall thickness of the upper airways, trachea, and bronchial tree
δt	Time increment

η_{WG} Dynamic viscosity of the water/glycerin mixture
λ Wavelength of the Darwin-Duo laser
ν Kinematic viscosity
Ω Anti-symmetric rate-of-rotation tensor
ω Collision frequency
Ψ Symmetric rate-of-strain tensor
ρ Fluid density
ρ_{outl} Density at all outlets
ρ_{WG} Density of the water/glycerin mixture
ρ_0 Reference density
ξ Discrete molecular velocity

REFERENCES

[1]Institute of Aerodynamics, RWTH Aachen University (2024). "Multiphysics - Aerodynamisches Institut Aachen (M-AIA)," Zenodo. https://doi.org/10.5281/zenodo.13350585
[2]Aljawad, H., Rüttgers, M., Lintermann, A., Schröder, W., and Lee, K., "Effects of the nasal cavity complexity on the pharyngeal airway fluid mechanics: A computational study," J. Digital Imaging **34**, 1120–1133 (2021).
[3]Antiga, L., Piccinelli, M., Botti, L., Ene-Iordache, B., Remuzzi, A., and Steinman, D. A., "An image-based modeling framework for patient-specific computational hemodynamics," Med. Biol. Eng. Comput. **46**, 1097–1112 (2008).
[4]Asgharian, B., Hofmann, W., and Bergmann, R., "Particle deposition in a multiple-path model of the human lung," Aerosol Sci. Technol. **34**, 332–339 (2001).
[5]Bouzidi, M., Firdaouss, M., and Lallemand, P., "Momentum transfer of a Boltzmann-lattice fluid with boundaries," Phys. Fluids **13**(11), 3452–3459 (2001).
[6]Calmet, H., Gambaruto, A., Bates, A., Vázquez, M., Houzeaux, G., and Doorly, D., "Large-scale CFD simulations of the transitional and turbulent regime for the large human airways during rapid inhalation," Comput. Biol. Med. **69**, 166–180 (2015).
[7]Carson, J. M., Van Loon, R., and Arora, H., "A personalised computational model of the impact of COVID-19 on lung function under mechanical ventilation," Comput. Biol. Med. **183**, 109177 (2024).
[8]Chen, J. and Gutmark, E., "Numerical investigation of airflow in an idealized human extra-thoracic airway: A comparison study," Biomech. Model. Mechanobiol. **13**, 205–214 (2013).
[9]Dastoorian, F., Pakzad, L., Kozinski, J., and Behzadfar, E., "A CFD investigation on the aerosol drug delivery in the mouth–throat airway using a pressurized metered-dose inhaler device," Processes **10**(7), 1230 (2022).
[10]De Backer, J. D., Vos, W., Gorlé, C., Germonpré, P., Partoens, B., Wuyts, F. L., Parizel, P., and Backer, W. D., "Flow analyses in the lower airways: Patient-specific model and boundary conditions," Med. Eng. Phys. **30**(7), 872–879 (2008).
[11]Dean, W. R. and Hurst, J. M., "Note on the motion of fluid in a curved pipe," Mathematika **6**(1), 77–85 (1959).
[12]Doty, R. L., "Olfaction," Annu. Rev. Psychol. **52**, 423–452 (2001).
[13] Dubief, Y. and Delcayre, F., "On coherent-vortex identification in turbulence," J. Turbul. **1**, N11 (2000).
[14]Dutta, R., Spence, B., Wei, X., Dhapare, S., Hindle, M., and Longest, P., "CFD guided optimization of nose-to-lung aerosol delivery in adults: Effects of inhalation waveforms and synchronized aerosol delivery," Pharm. Res. **37**, 199 (2020).
[15]Emmerling, J., Vahaji, S., Morton, D. A., Fletcher, D. F., and Inthavong, K., "Scale resolving simulations of the effect of glottis motion and the laryngeal jet on flow dynamics during respiration," Comput. Methods Programs Biomed. **247**, 108064 (2024).
[16]Farkas, Á., Lizal, F., Jedelsky, J., Elcner, J., Karas, J., Belka, M., Misik, O., and Jicha, M., "The role of the combined use of experimental and computational methods in revealing the differences between the micron-size particle deposition patterns in healthy and asthmatic subjects," J. Aerosol Sci. **147**, 105582 (2020).
[17]Fresconi, F. E. and Prasad, A. K., "Secondary velocity fields in the conducting airways of the human lung," J. Biomech. Eng. **129**(5), 722–732 (2007).
[18]Gaddam, M. G. and Santhanakrishnan, A., "Effects of varying inhalation duration and respiratory rate on human airway flow," Fluids **6**(6), 221 (2021).
[19]Geller, S., Krafczyk, M., Tölke, J., Turek, S., and Hron, J., "Benchmark computations based on lattice-Boltzmann, finite element and finite volume methods for laminar flows," Comput. Fluids **35**(8), 888–897 (2006).
[20]Haight, J. S. J. and Cole, P., "The site and function of the nasal valve," Laryngoscope **93**(1), 49–55 (1983).
[21]Hartmann, D., Meinke, M., and Schröder, W., "An adaptive multilevel multigrid formulation for Cartesian hierarchical grid methods," Comput. Fluids **37**(9), 1103–1125 (2008).
[22]He, X. and Luo, L.-S., "Theory of the lattice Boltzmann method: From the Boltzmann equation to the lattice Boltzmann equation," Phys. Rev. E **56**(6), 6811–6817 (1997).
[23]Hörschler, I., Schröder, W., and Meinke, M., "On the assumption of steadiness of nasal cavity flow," J. Biomech. **43**(6), 1081–1085 (2010).
[24]Johanning-Meiners, B. H., Mayolle, L., Schröder, W., and Klaas, M., "3D Lagrangian particle tracking in a model of the human airways," in *Proceedings of the International Symposium on the Application of Laser and Imaging Techniques to Fluid Mechanics* (Springer, 2024), Vol. 21, pp. 1–13.
[25]Johanning-Meiners, B. H., Schier, C., Meyer, T., Dörner, P., Gruhlke, M., Schröder, W., and Klaas, M., "Combined velocity and aerosol deposition measurements in the respiratory tract using HS-PIV and MTT assay," in 15th International Symposium on Particle Image Velocimetry (2023), see https://scholarworks.calstate.edu/downloads/qb98mn684.
[26]Johari, N., Osman, K., Helmi, N., and Abdul Kadir, M., "Comparative analysis of realistic CT-scan and simplified human airway models in airflow simulation," Comput. Methods Biomech. Biomed. Eng. **18**, 48 (2015).
[27]Keck, T., Leiacker, R., Heinrich, A., Kühnemann, S., and Rettinger, G., "Humidity and temperature profile in the nasal cavity," Rhinology **38**, 167–171 (2001).
[28]Kelly, J. T., Prasad, A. K., and Wexler, A. S., "Detailed flow patterns in the nasal cavity," J. Appl. Physiol. **89**(1), 323–337 (2000).
[29]Krebs, F., Silva, F., Sciamarella, D., and Artana, G., "A three-dimensional study of the glottal jet," Exp. Fluids **52**, 1133 (2012).
[30]Li, C., Jiang, J., Dong, H., and Zhao, K., "Computational modeling and validation of human nasal airflow under various breathing conditions," J. Biomech. **64**, 59–68 (2017).
[31]Li, J., Liao, W.-K., Choudhary, A., Ross, R., Thakur, R., Gropp, W., Latham, R., Siegel, A., Gallagher, B., and Zingale, M., "Parallel netCDF: A high-performance scientific I/O interface," in *SC'03: Proceedings of the 2003 ACM/IEEE Conference on Supercomputing* (IEEE, 2003), p. 39.
[32]Lintermann, A., Meinke, M., and Schröder, W., "Investigations of human nasal cavity flows based on a lattice-Boltzmann method," in *High Performance Computing on Vector Systems 2011*, edited by Resch, M., Wang, X., Bez, W., Focht, E., Kobayashi, H., and Roller, S. (Springer Berlin Heidelberg, Berlin, Heidelberg, 2012), pp. 143–158.
[33]Lintermann, A., Meinke, M., and Schröder, W., "Fluid mechanics based classification of the respiratory efficiency of several nasal cavities," Comput. Biol. Med. **43**(11), 1833–1852 (2013).
[34]Lintermann, A., Schlimpert, S., Grimmen, J. H., Günther, C., Meinke, M., and Schröder, W., "Massively parallel grid generation on HPC systems," Comput. Methods Appl. Mech. Eng. **277**, 131–153 (2014).
[35]Lintermann, A. and Schröder, W., "Simulation of aerosol particle deposition in the upper human tracheobronchial tract," Eur. J. Mech. B **63**, 73–89 (2017).
[36]Lintermann, A. and Schröder, W., "A hierarchical numerical journey through the nasal cavity: From nose-like models to real anatomies," Flow, Turbul. Combust. **102**, 89–102 (2019).
[37]Liu, X., Rüttgers, M., Quercia, A., Egele, R., Pfaehler, E., Shende, R., Aach, M., Schröder, W., Balaprakash, P., and Lintermann, A., "Refining computer tomography data with super-resolution networks to increase the accuracy of respiratory flow simulations," Future Gener. Comput. Syst. **159**, 474–488 (2024).
[38]Lizal, F., Elcner, J., Hopke, P., Jedelsky, J., and Jicha, M., "Development of a realistic human airway model," Proc. Inst. Mech. Eng. H **226**, 197–207 (2012).

[39]Lizal, F., Elcner, J., Jedelsky, J., Maly, M., Jicha, M., Farkas, Á., Belka, M., Rehak, Z., Adam, J., Brinek, A., Laznovsky, J., Zikmund, T., and Kaiser, J., "The effect of oral and nasal breathing on the deposition of inhaled particles in upper and tracheobronchial airways," J. Aerosol Sci. **150**, 105649 (2020).
[40]Loring, S., Garcia-Jacques, M., and Malhotra, A., "Pulmonary characteristics in COPD and mechanisms of increased work of breathing," J. Appl. Physiol. **107**, 309–314 (2009).
[41]Luo, X., Hinton, J., Liew, T., and Tan, K., "LES modelling of flow in a simple airway model," Med. Eng. Phys. **26**(5), 403–413 (2004).
[42]McNeel, R. *et al.*, *Rhinoceros 3D, Version 6.0* (Robert McNeel & Associates, Seattle, WA, 2010).
[43]Mittal, R., Erath, B., and Plesniak, M., "Fluid dynamics of human phonation and speech," Annu. Rev. Fluid Mech. **45**, 437–467 (2013).
[44]Morita, K., Takeishi, N., Wada, S., and Hatakeyama, T., "Computational fluid dynamics assessment of congenital tracheal stenosis," Pediatr. Surg. Int. **38**, 1769 (2022).
[45]Morton, G., *A Computer Oriented Geodetic Data Base and a New Technique in File Sequencing* (International Business Machines Company, 1966).
[46]Niegodajew, P., "Flow patterns and vortex formation mechanisms inside a human nasal cavity," Phys. Fluids **37**(2), 021918 (2025).
[47]Putz, R., Pabst, R., Putz, R., and Weiglein, A. H., *Atlas of Human Anatomy Sobotta* (Lippincott Williams & Wilkins, 2001).
[48]Qian, Y. H., D'Humières, D., and Lallemand, P., "Lattice BGK models for Navier-Stokes equation," Europhys. Lett. **17**(6), 479–484 (1992).
[49]Reynolds, O., "An experimental investigation of the circumstances which determine whether the motion of water shall be direct or sinuous, and of the law of resistance in parallel channels," Philos. Trans. R. Soc. London **174**(1883), 935–982 (1883).
[50]Rüttgers, M., Hübenthal, F., Tsubokura, M., and Lintermann, A., "Parallel reinforcement learning and Gaussian process regression for improved physics-based nasal surgery planning," in *Parallel Processing and Applied Mathematics*, edited by Wyrzykowski, R., Dongarra, J., Deelman, E., and Karczewski, K. (Springer Nature Switzerland, Cham, 2025), pp. 79–96.
[51]Rüttgers, M., Waldmann, M., Schröder, W., and Lintermann, A., "Machine-learning-based control of perturbed and heated channel flows," in *High Performance Computing*, edited by Jagode, H., Anzt, H., Ltaief, H., and Luszczek, P. (Springer International Publishing, Cham, 2021), pp. 7–22.
[52]Rüttgers, M., Waldmann, M., Hübenthal, F., Vogt, K., Tsubokura, M., Lee, S., and Lintermann, A., "Towards a widespread usage of computational fluid dynamics simulations for automated virtual nasal surgery planning," Future Gener. Comput. Syst. **174**, 107935 (2025).
[53]Rüttgers, M., Waldmann, M., Schröder, W., and Lintermann, A., "A machine-learning-based method for automatizing lattice-Boltzmann simulations of respiratory flows," Appl. Intell. **52**, 9080–9100 (2022).
[54]Rüttgers, M., Waldmann, M., Vogt, K., Ilgner, J., Schröder, W., and Lintermann, A., "Automated surgery planning for an obstructed nose by combining computational fluid dynamics with reinforcement learning," Comput. Biol. Med. **173**, 108383 (2024).
[55]Sadafi, H., Tousi, N., Backer, W., and Backer, J., "Validation of computational fluid dynamics models for airway deposition with SPECT data of the same population," Sci. Rep. **14**, 5492 (2024).
[56]Sagan, H., *Hilbert's Space-Filling Curve* (Springer New York, New York, NY, 1994), pp. 9–30.
[57]Saksono, P. H., Nithiarasu, P., Sazonov, I., and Yeo, S. Y., "Computational flow studies in a subject-specific human upper airway using a one-equation turbulence model. Influence of the nasal cavity," Int. J. Numer. Methods Eng. **87**(1–5), 96–114 (2011).
[58]Sarangapani, R., "Modeling particle deposition in extrathoracic airways," Aerosol Sci. Technol. **32**(1), 72–89 (2000).
[59]Schanz, D., Gesemann, S., and Schröder, A., "Shake-the-box: Lagrangian particle tracking at high particle image densities," Exp. Fluids **57**(5), 70 (2016).
[60]Schillaci, A. and Quadrio, M., "Importance of the numerical schemes in the CFD of the human nose," J. Biomech. **138**, 111100 (2022).
[61]Schlichting, H. and Gersten, K., *Boundary-Layer Theory*, 9th ed. (Springer, Berlin, Heidelberg, 2016).
[62]Schröder, A., Willert, C., Schanz, D., Geisler, R., Jahn, T., Gallas, Q., and Leclaire, B., "The flow around a surface mounted cube: A characterization by time-resolved PIV, 3D Shake-The-Box and LBM simulation," Exp. Fluids **61**(9), 189 (2020).
[63]Shao, J., Yan, W., Liu, Y., and Lu, M., "Flow simulation in the upper respiratory tract of two obstructive sleep apnea patients with successful and failed surgery," Comput. Math. Methods Med. **2021**, 1–12.
[64]Shinwari, D., Scherer, R. C., DeWitt, K. J., and Afjeh, A. A., "Flow visualization and pressure distributions in a model of the glottis with a symmetric and oblique divergent angle of 10 degrees," J. Acoust. Soc. Am. **113**(1), 487–497 (2003).
[65]Siemens Digital Industries Software, *Simcenter STAR-CCM+ User Guide v. 2012* (Siemens, 2012).
[66]Sommerfeld, M., Sgrott, O., Taborda, M., Koullapis, P., Bauer, K., and Kassinos, S., "Analysis of flow field and turbulence predictions in a lung model applying rans and implications for particle deposition," Eur. J. Pharm. Sci. **166**, 105959 (2021).
[67]Srivastava, V. K. and Anand, A. R., "Analysis of 2D human airway in laminar and turbulent flow model," in *Fluid Mechanics and Fluid Power*, edited by Singh, K. M., Dutta, S., Subudhi, S., and Singh, N. K. (Springer Nature Singapore, Singapore, 2024), Vol. 4, pp. 855–863.
[68]Stylianou, F. S., Sznitman, J., and Kassinos, S. C., "Direct numerical simulation of particle laden flow in a human airway bifurcation model," Int. J. Heat Fluid Flow **61**, 677–710 (2016).
[69]Thörnig, P., "JURECA: Data Centric and Booster Modules implementing the Modular Supercomputing Architecture at Jülich Supercomputing Centre," J. Large-Scale Res. Facil. **7**, A182 (2021).
[70]Titze, I., "Nonlinear source-filter coupling in phonation: Theory," J. Acoust. Soc. Am. **123**, 2733–2749 (2008).
[71]Tsega, E., "CFD simulations of respiratory airflow in human upper airways response to walking and running for oral breathing condition," Heliyon **8**, e10039 (2022).
[72]Waldmann, M., Grosch, A., Witzler, C., Lehner, M., Benda, O., Koch, W., Vogt, K., Kohn, C., Schröder, W., Göbbert, J., and Lintermann, A., "An effective simulation- and measurement-based workflow for enhanced diagnostics in rhinology," Med. Biol. Eng. Comput. **60**, 365 (2022).
[73]Waldmann, M., Lintermann, A., Choi, Y. J., and Schröder, W., "Analysis of the effects of MARME treatment on respiratory flow using the lattice-Boltzmann method," in *New Results in Numerical and Experimental Fluid Mechanics XII*, edited by Dillmann, A., Heller, G., Krämer, E., Wagner, C., Tropea, C., and Jakirlić, S. (Springer International Publishing, Cham, 2020), pp. 853–863.
[74]Waldmann, M., Rüttgers, M., Lintermann, A., and Schröder, W., "Virtual surgeries of nasal cavities using a coupled lattice-Boltzmann–level-set approach," J. Eng. Sci. Med. Diagn. Ther. **5**(3), 031104 (2022).
[75]Wei, J., He, X., Yang, Q., Gu, Q., Zhang, X., Sui, X., Zhou, R., and Feng, W., "Numerical simulation of the influence of nasal cycle on nasal airflow," Sci. Rep. **14**, 12161 (2024).
[76]Xu, X., Wu, J., Weng, W., and Fu, M., "Investigation of inhalation and exhalation flow pattern in a realistic human upper airway model by PIV experiments and CFD simulations," Biomech. Model. Mechanobiol. **19**, 1679 (2020).
[77]Yang, M., Higano, N., Gunatilaka, C., Hysinger, E., Amin, R., Woods, J., and Bates, A., "Subglottic stenosis position affects work of breathing," Laryngoscope **131**, E1220–E1226 (2021).
[78]Zhang, Z., Kleinstreuer, C., and Kim, C. S., "Effects of curved inlet tubes on air flow and particle deposition in bifurcating lung models," J. Biomech. **34**, 659–669 (2001).
[79]Zhao, K., Dalton, P., Yang, G., and Scherer, P., "Numerical modeling of turbulent and laminar airflow and odorant transport during sniffing in the human and rat nose," Chem. Senses **31**, 107–118 (2006).
[80]Zuber, M., Abdullah, M., Ismail, R., Shuaib, I. L., Sheikh Ab Hamid, S., and Ahmad, K., "Review: A critical overview of limitations of CFD modeling in nasal airflow," J. Med. Biol. Eng. **32**, 77–84 (2012).
[81]Zwicker, D., Ostilla-Mónico, R., Lieberman, D., and Brenner, M., "Physical and geometric constraints explain the labyrinth-like shape of the nasal cavity," Proc. Natl. Acad. Sci. U. S. A. **115**, 2936 (2018).